

1 LEVERAGING MULTI-MESSENGER ASTROPHYSICS FOR DARK MATTER SEARCHES

By

Daniel Nicholas Salazar-Gallegos

A DISSERTATION

Submitted to
Michigan State University
in partial fulfillment of the requirements
for the degree of

Physics—Doctor of Philosophy
Computational Mathematics in Science and Engineering—Dual Major

Today

ABSTRACT

3 I did Dark Matter with HAWC and IceCube. I also used Graph Neural Networks

⁴ Copyright by

⁵ DANIEL NICHOLAS SALAZAR-GALLEGOS

⁶ Today

ACKNOWLEDGMENTS

8 I love my friends. Thanks to everyone that helped me figure this out. Amazing thanks to the people
9 at LANL who supported me. Eames, etc Dinner Parties Jenny and her child Kaydince Kirsten, Pat,
10 Andrea Family. You're so far but so critical to my formation. Unconditional love. Roommate

TABLE OF CONTENTS

12

LIST OF TABLES

13

Proof I know how to include

LIST OF FIGURES

LIST OF ABBREVIATIONS

- 16 **MSU** Michigan State University
- 17 **LANL** Los Alamos National Laboratory
- 18 **DM** Dark Matter
- 19 **SM** Standard Model
- 20 **HAWC** High Altitude Water Cherenkov Observatory

CHAPTER 1

INTRODUCTION

22 Is the text not rendering right? Ah ok it knows im basically drafting the doc still

CHAPTER 2

23

DARK MATTER IN THE COSMOS

24 **2.1 Introduction**

25 The dark matter problem can be summarized in part by the following thought experiment.

26 Let us say you are the teacher for an elementary school classroom. You take them on a field
27 trip to your local science museum and among the exhibits is one for mass and weight. The exhibit
28 has a gigantic scale, and you come up with a fun problem for your class.

29 You ask your class, "What is the total weight of the classroom? Give your best estimation to
30 me in 30 minutes, and then we'll check your guess on the scale. If your guess is within 10% of the
31 right answer, we will stop for ice cream on the way back."

32 The students are ecstatic to hear this, and they get to work. The solution is some variation of
33 the following strategy. The students should give each other their weight or best guess if they do
34 not know. Then, all they must do is add each student's weight and get a grand total for the class.
35 The measurement on the giant scale should show the true weight of the class. When comparing
36 the measured weight to your estimation, multiply the measurement by 1.0 ± 0.1 to get the $\pm 10\%$
37 tolerances for your estimation.

38 Two of your students, Sandra and Mario, return to you with a solution.

39 They say, "We weren't sure of everyone's weight. We used 65 lbs. for the people we didn't
40 know and added everyone who does know. There are 30 of us, and we got 2,000 lbs.! That's a ton!"

41 You estimated 1,900 lbs. assuming the average weight of a student in your class was 60 lbs.
42 So, you are pleased with Sandra's and Mario's answer. You instruct your students to all gather on
43 the giant scale and read off the weight together. To all your surprise, the scale reads *10,000 lbs.*!
44 10,000 is significantly more than a 10% error from 2,000. In fact, it is approximately 5 times more
45 massive than either your or your students' estimates. You think to yourself and conclude there
46 must be something wrong with the scale. You ask an employee to check the scale and verify it is
47 well calibrated. They confirm that the scale is in working order. You weigh a couple of students
48 individually to assess that the scale is well calibrated. Sandra weighs 59 lbs., and Mario weighs

49 62 lbs., typical weights for their age. You then weigh each student individually and see that their
50 weights individually do not deviate greatly from 60 lbs. So, where does all the extra weight come
51 from?

52 This thought experiment serves as an analogy to the Dark Matter problem. The important
53 substitution to make however is to replace the students with stars and the classroom with a galaxy,
54 say the Milky Way. Individually the mass of stars is well measured and defined with the Sun as our
55 nearest test case. However, when we set out to measure the mass of a collection of stars as large as
56 galaxies, our well-motivated estimation is wildly incorrect. There simply is no way to account for
57 this discrepancy except without some unseen, or dark, contribution to mass and matter in galaxies.
58 I set out in my thesis to narrow the possibilities of what this Dark Matter could be.

59 This chapter is organized like the following... **TODO: Text should look like ... Chapter x has**
60 **blah blah blah.**

61 2.2 Dark Matter Basics

62 Presently, a more compelling theory of cosmology that includes Dark Matter (DM) in order
63 to explain a variety of observations is Λ Cold Dark Matter, or Λ CDM. I present the evidence
64 supporting Λ CDM in ?? yet discuss the conclusions of the Λ CDM model here. According to
65 Λ CDM fit to observations on the Cosmic Microwave Background (CMB), DM is 26.8% of the
66 universe's current energy budget. Baryonic matter, stuff like atoms, gas, and stars, contributes to
67 4.9% of the universe's current energy budget [1, 2, 3].

68 DM is dark; it does not interact readily with light at any wavelength. DM also does not interact
69 noticeably with the other standard model forces (Strong and Weak) at a rate that is readily observed
70 [3]. DM is cold, which is to say that the average velocity of DM is below relativistic speeds [1].
71 'Hot' DM would not likely manifest the dense structures we observe like galaxies, and instead
72 would produce much more diffuse galaxies than what is observed [3, 1]. DM is old; it played a
73 critical role in the formation of the universe and the structures within it [1, 2].

74 Observations of DM have so far been only gravitational. The parameter space available to what
75 DM could be therefore is extremely broad. The broad DM parameter space is iteratively tested in

76 DM searches by supposing a hypothesis that has not yet been ruled out and performing observations
77 to test them. When the observations yield a null result, the parameter space is constrained further.
78 I present some approaches for DM searches in ??.

79 **2.3 Evidence for Dark Matter**

80 Dark Matter (DM) has been a looming problem in physics for almost 100 years. Anomalies
81 have been observed by astrophysicists in galactic dynamics as early as 1933 when Fritz Zwicky
82 noticed unusually large velocity dispersion in the Coma cluster. Zwicky's measurement was the
83 first recorded to use the Virial theorem to measure the mass fraction of visible and invisible matter
84 in celestial bodies [4]. From Zwicky in [5], "*If this would be confirmed, we would get the surprising*
85 *result that dark matter is present in much greater amount than luminous matter.*" Zwicky's and
86 others' observation did not instigate a crisis in astrophysics because the measurements did not
87 entirely conflict with their understanding of galaxies [4]. In 1978, Rubin, Ford, and Norbert
88 measured rotation curves for ten spiral galaxies [6]. Rubin et al.'s 1978 publication presented a
89 major challenge to the conventional understanding of galaxies that could no longer be dismissed by
90 measurement uncertainties. Evidence has been mounting ever since for this exotic form of matter.
91 The following subsections provide three compelling pieces of evidence in support of the existence
92 of DM.

93 **2.3.1 First Clues: Stellar Velocities**

94 Zwicky, and later Rubin, measured the stellar velocities of various galaxies to estimate their
95 virial mass. The Virial Theorem upon which these observations are interpreted is written as

$$2T + V = 0. \quad (2.1)$$

96 Where T is the kinetic energy and V is the potential energy in a self-gravitating system. The
97 classical Newton's law of gravity from stars and gas was used for gravitational potential modeled in
98 the observed galaxies:

$$V = -\frac{1}{2} \sum_i \sum_{j \neq i} \frac{m_i m_j}{r_{ij}}. \quad (2.2)$$

99 Zwicky et al. measured just the velocities of stars apparent in optical wavelengths [5]. Rubin et al.
 100 added by measuring the velocity of the hydrogen gas via the 21 cm emission line of Hydrogen [6].
 101 The velocities of the stars and gas are used to infer the total mass of galaxies and galaxy clusters via
 102 ???. An inferred mass is obtained from the luminosity of the selected sources. The two inferences
 103 are compared to each other as a luminosity to mass ratio which typically yielded [1]

$$\frac{M}{L} \sim 400 \frac{M_{\odot}}{L_{\odot}} \quad (2.3)$$

104 M_{\odot} and L_{\odot} referring to stellar mass and stellar luminosity, respectively. These ratios clearly indicate
 105 a discrepancy in apparent light and mass from stars and gas and their velocities.

106 Rubin et al. [6] demonstrated that the discrepancy was unlikely to be an underestimation of
 107 the mass of the stars and gas. The inferred "dark" mass was up to 5 times more than the luminous
 108 mass. This dark mass also needed to extend well beyond the extent of the luminous matter.

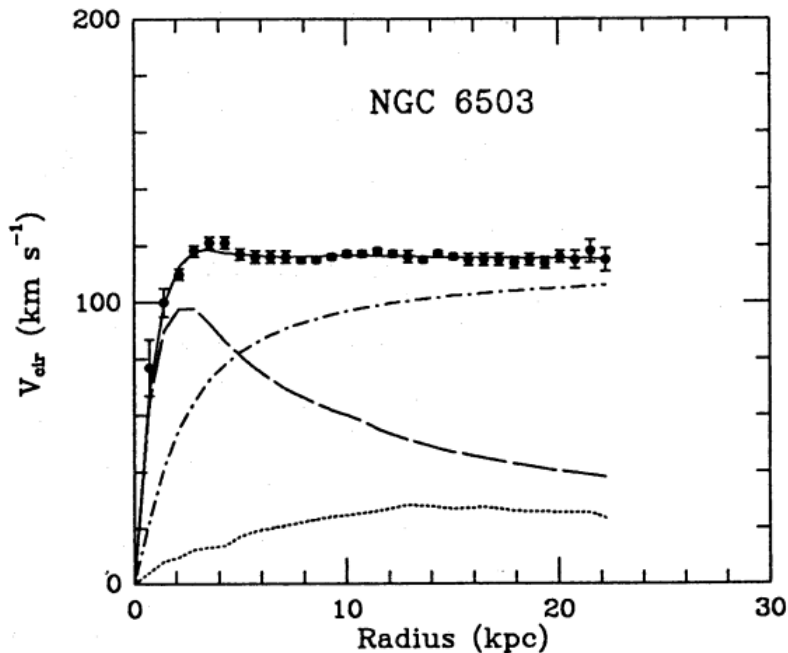


Figure 2.1 Rotation curve fit to NGC 6503 from [7]. Dashed line is the contribution from visible matter. Dotted curves are from gas. Dash-dot curves are from dark matter (DM). Solid line is the composite contribution from all matter and DM sources. Data are indicated with bold dots with error bars. Data agree strongly with a matter + DM composite prediction.

109 ?? features one of many rotation curves plotted from the stellar velocities within galaxies. The

110 measured rotation curves mostly feature a flattening of velocities at higher radius which is not
111 expected if the gravity was only coming from gas and luminous matter. The extension of the
112 flat velocity region also indicates that the DM is distributed far from the center of the galaxy.
113 Modern velocity measurements include significantly larger objects, galactic clusters, and smaller
114 objects, dwarf galaxies. Yet, measurements along this regime are leveraging the Virial theorem
115 with Newtonian potential energies. We know Newtonian gravity is not a comprehensive description
116 of gravity. New observational techniques have been developed since 1978, and those are discussed
117 in the following sections.

118 **2.3.2 Evidence for Dark Matter: Gravitational Lensing**

119 Modern evidence for dark matter comes from new avenues beyond stellar velocities. Grav-
120 itational lensing from DM is a new channel from general relativity. General relativity predicts
121 aberrations in light caused by massive objects. In recent decades we have been able to measure
122 the lensing effects from compact objects and DM halos. ?? shows how different massive objects
123 change the final image of a faraway galaxy resulting from gravitational lensing. Gravitational
124 lensing developed our understanding of dark matter in two important ways.

125 Gravitational lensing provides additional compelling evidence for DM. The observation of two
126 merging galactic clusters in 2006, shown in ??, provided a compelling argument for DM outside
127 the Standard Model. These clusters merged recently in astrophysical time scales. Galaxies and
128 star cluster have mostly passed by each other as the likelihood of their collision is low. Therefore,
129 these massive objects will mostly track the highest mass, dark and/or baryonic, density. Yet, the
130 intergalactic gas is responsible for the majority of the baryonic mass in the systems [4]. These gas
131 bodies will not phase through and will heat up as they collide together. The hot gas is located via
132 x-ray emission from the cluster. Two observations of the clusters were performed independently of
133 each other.

134 The first was the lensing of light around the galaxies due to their gravitational influences. When
135 celestial bodies are large enough, the gravity they exert bends space and time itself. The warped
136 space-time lenses light and will deflect in an analogous way to how glass lenses will bend light, see

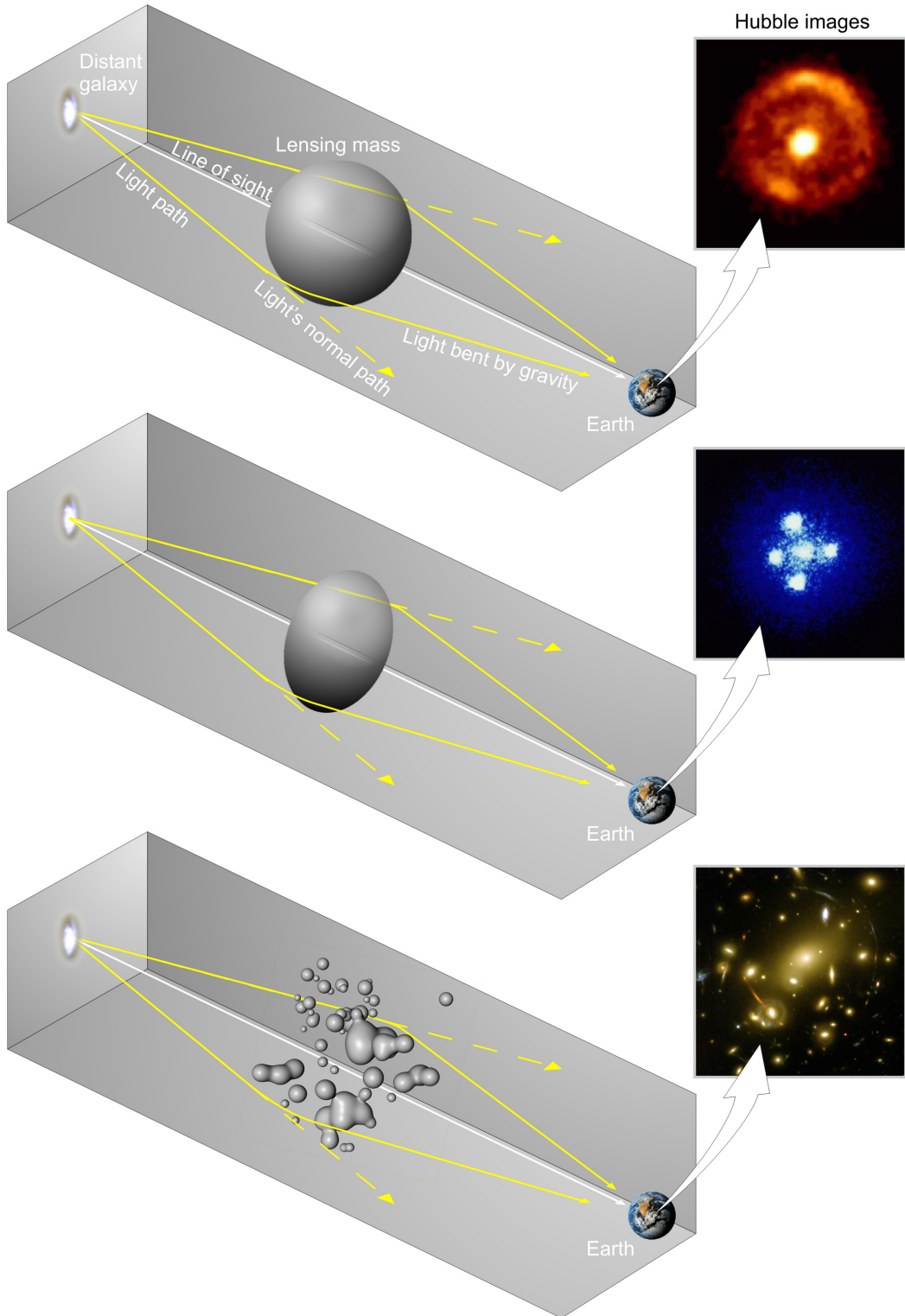


Figure 2.2 Light from distant galaxy is bent in unique ways depending on the distribution of mass between the galaxy and Earth. Yellow dashed lines indicate where the light would have gone if the matter were not present [8].

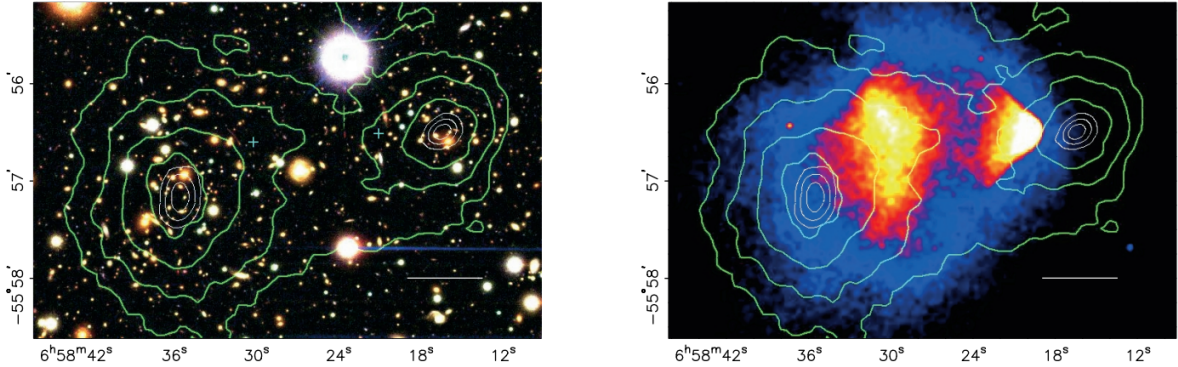


Figure 2.3 (left) Optical image of galactic cluster 1E0657-558. (right) X-ray image of the cluster with redder meaning hotter and higher baryon density. (both) Green contours are reconstruction of gravity contours from weak lensing. White rings are the best fit mass maxima at 68.3%, 95.5%, and 99.7% confidence. The matter maxima of the clusters are clearly separated from x-ray maxima. [9]

137 ???. With a sufficient understanding of light sources behind a massive object, we can reconstruct
 138 the contours of the gravitational lenses. The gradient of the contours shown in ?? then indicates
 139 how dense the matter is and where it is.

140 The x-ray emission can then be observed from the clusters. Since these galaxies are mostly gas
 141 and are merging, then the gas should be getting hotter. If they are merging, the x-ray emissions
 142 should be the strongest where the gas is mostly moving through each other. Hence, X-ray emission
 143 maps out where the gas is in the merging galaxy cluster.

144 The lensing and x-ray observations were done on the Bullet cluster featured on ???. The x-ray
 145 emissions do not align with the gravitational contours from lensing. The incongruence in mass
 146 density and baryon density suggests that there is a lot of matter somewhere that does not interact
 147 with light. Moreover, this dark matter cannot be baryonic [9]. The Bullet Cluster measurement did
 148 not really tell us what DM is exactly, but it did give the clue that DM also does not interact with
 149 itself very strongly. If DM did interact strongly with itself, then it would have been more aligned
 150 with the x-ray emission [9]. There have been follow-up studies of galaxy clusters with similar
 151 results. The Bullet Cluster and others like it provide a persuasive case against something possibly
 152 amiss in our gravitational theories.

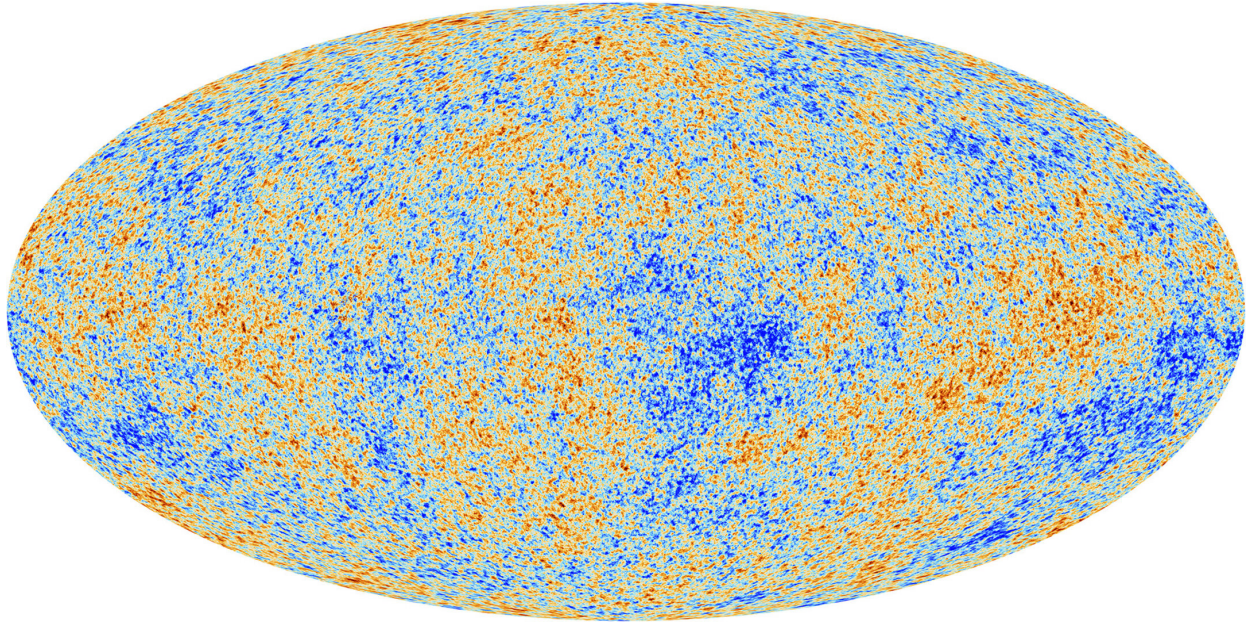


Figure 2.4 Plank CMB sky. Sky map features small variations in temperature in primordial light. These anisotropies are used to make inferences about the universe’s energy budget and developmental history. [10]

153 **2.3.3 Evidence for Dark Matter: Cosmic Microwave Background**

154 The Cosmic Microwave Background (CMB) is the primordial light from the early universe
155 when Hydrogen atoms formed from the free electron and proton soup in the early universe. The
156 CMB is the earliest light we can observe; released when the universe was about 380,000 years old.
157 Then we look at how the simulated universes look like compared to what we see. ?? is the most
158 recent CMB image from the Plank satellite after subtracting the average value and masking the
159 galactic plane [10]. Redder regions indicate a slightly hotter region in the CMB, and blue indicates
160 colder. The intensity variations are on the order of 1 in 1000 with respect to the average value.

161 The Cosmic Microwave Background shows that the universe had DM in it from an incredibly
162 early stage. To measure the DM, Dark Energy, and matter fractions of the universe from the CMB,
163 the image is analyzed into a power spectrum, which shows the amplitude of the fluctuations as
164 a function of spherical multipole moments. Λ CDM provides the best fit to the power spectra of
165 the CMB as shown in ?. The CMB power spectrum is quite sensitive to the fraction of each
166 energy contribution in the early universe. Low l modes are dominated by variations in gravitational
167 potential. Intermediate l emerge from oscillations in photon-baryon fluid from competing baryon

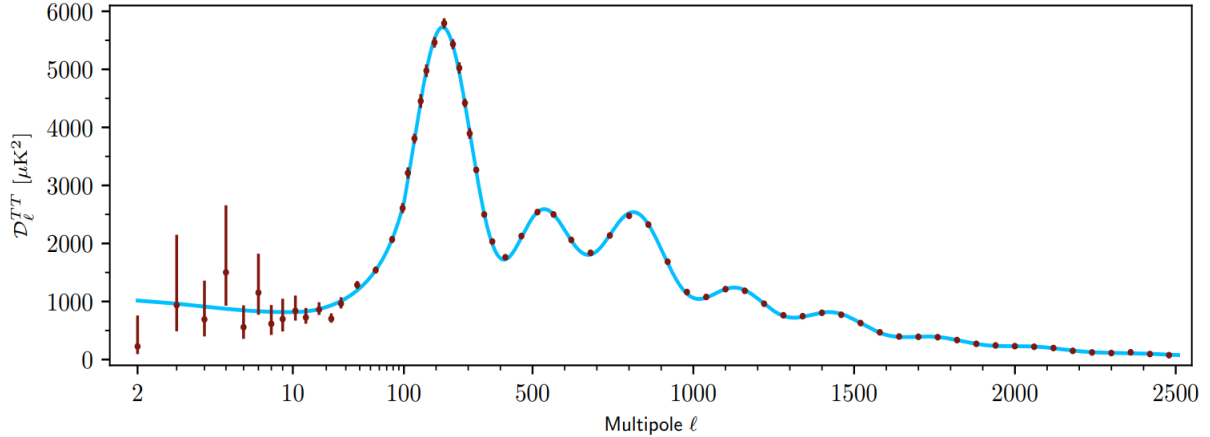


Figure 2.5 Observed Cosmic Microwave Background power spectrum as a function of multipole moment from Plank [10]. Blue line is best fit model from Λ CDM. Red points and lines are data and error, respectively.

168 pressures and gravity. High l is a damped region from the diffusion of photons during electron-
169 proton recombination. [1]

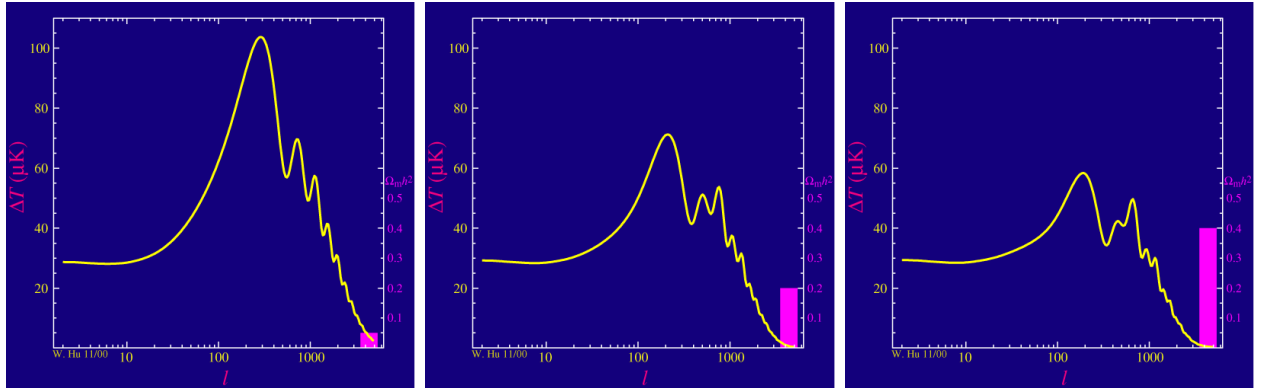


Figure 2.6 Predicted power spectra of CMB for different $\Omega_m h^2$ values for fixed baryon density from [11]. (left) Low $\Omega_m h^2$ increases the prominence of first and second peaks. (middle) $\Omega_m h^2$ is most similar to the observed power spectrum. The second and third peaks are similar in height. (right) $\Omega_m h^2$ is large which suppresses the first peak and raises the prominence of the third peak.

170 The harmonics would look quite different for a universe with less DM. ?? demonstrates the
171 effect $\Omega_m h^2$ has on the expected power spectrum for fixed baryon matter density. [11] Sweeping
172 $\Omega_m h^2$ in this way clearly shows the effect dark matter has on the CMB power spectrum. The
173 observations fit well with the Λ CDM model, and the derived fractions are as follows. The matter
174 fraction: $\Omega_m = 0.3153$; and the baryon fraction: $\Omega_b = 0.04936$ [10]. Plank's observations also
175 provide a measure of the Hubble constant, H_0 . H_0 especially has seen a growing tension in the

176 past decade that continues to deepened with observations from instruments like the James Webb
177 Telescope [12, 13]. As Hubble tensions deepen, we may find that perhaps Λ **CDM**, despite its
178 successes, is missing some critical physics.

179 Overall, the Newtonian motion of stars in galaxies, weak lensing from galactic clusters, and
180 power spectra from primordial light form a compelling body of research in favor of dark matter.
181 It takes another leap of theory and experimentation to make observations of DM that are non-
182 gravitational in nature. In ??, the evidence for DM implies strongly that the DM is matter and
183 not a lost parameter in the gravitational fields between massive objects. Finally, if we take one
184 axiom: that this matter has quantum behavior, such as being described by some Bohr wavelength
185 and abiding by some fermion or boson statistics; then we arrive at particle dark matter. One particle
186 DM hypothesis is the Weakly Interacting Massive Particle (WIMP). This DM candidate theory is
187 discussed further in the next section and is the focus of this thesis.

188 **2.4 Searching for Dark Matter: Particle DM**

189 ?? shows the Standard Model of particle physics and is currently the most accurate model for
190 the dynamics of fundamental particles like electrons and photons. The current status of the SM
191 does not have a viable DM candidate. When looking at the standard model, we can immediately
192 exclude any charged particle because charged particles interact strongly with light. Specifically,
193 this will rule out the following charged, fundamental particles: $e, \mu, \tau, W, u, d, s, c, t, b$ and their
194 corresponding antiparticles. Recalling from ?? that DM must be long-lived and stable over the
195 age of the universe which excludes all SM particles with decay half-lives at or shorter than the age
196 of the universe. The lifetime constraint additionally eliminates the Z and H bosons. Finally, the
197 candidate DM needs to be somewhat massive. Recall from ?? that DM is cold or not relativistic
198 through the universe. This eliminates the remaining SM particles: $\nu_{e,\mu,\tau}, g, \gamma$ as DM candidates.
199 Because there are no DM candidates within the SM, the DM problem strongly hints to physics
200 beyond the SM (BSM).

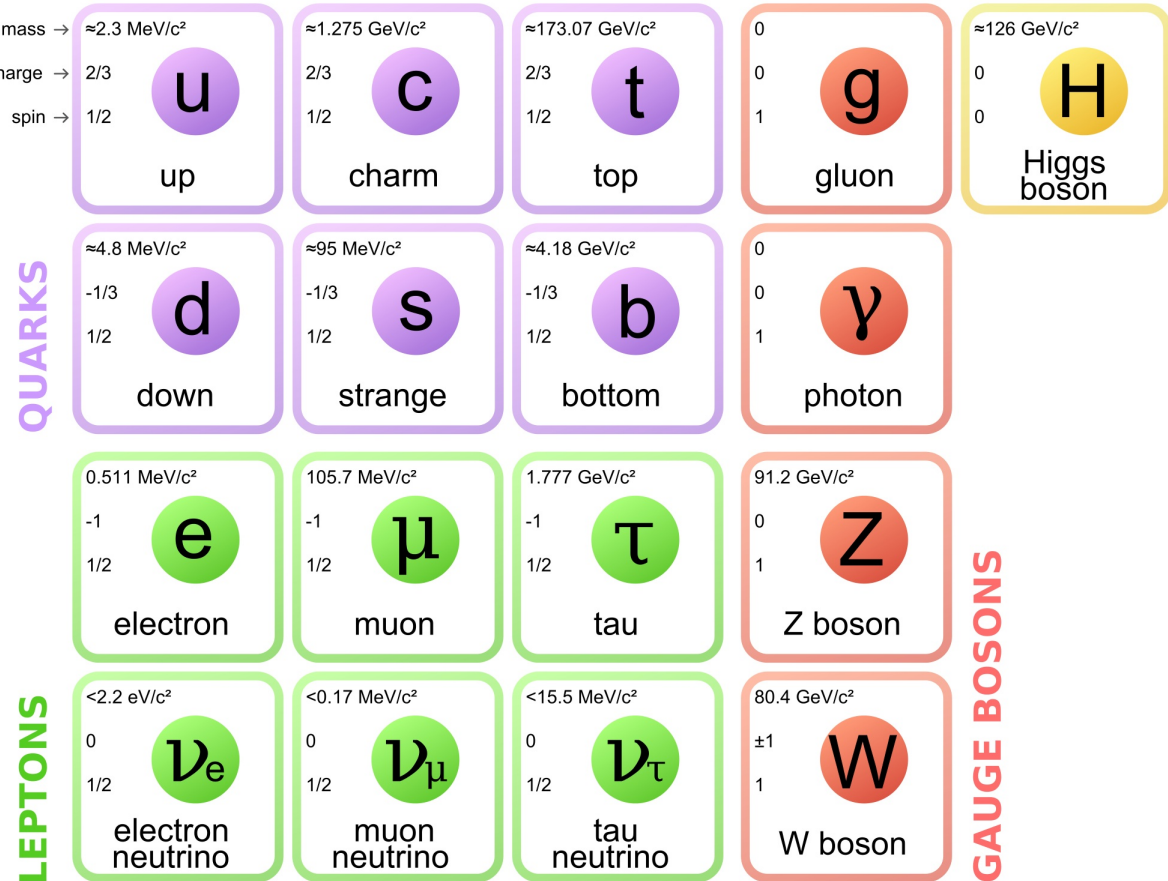


Figure 2.7 The Standard Model (SM) of particle physics. Figure taken from <http://www.quantumdiaries.org/2014/03/14/the-standard-model-a-beautiful-but-flawed-theory/>

201 2.4.1 Shake it, Break it, Make it

202 When considering DM that couples in some way with the SM, the interactions are roughly
 203 demonstrated by interaction demonstrated in ???. The figure is a simplified Feynman diagram
 204 where the arrow of time represents the interaction modes of: **Shake it, Break it, Make it.**

205 **Shake it** refers to the direct detection of dark matter. Direct detection interactions start with
 206 a free DM particle and an SM particle. The DM and SM interact via elastic or inelastic collision
 207 and recoil away from each other. The DM remains in the dark sector and imparts some momentum
 208 onto the SM particle. The hope is that the momentum imparted onto the SM particle is sufficiently
 209 high enough to pick up with extremely sensitive instruments. Because we cannot create the DM in
 210 the lab, a direct detection experiment must wait until DM is incident on the detector. Most direct
 211 detection experiments are therefore placed in low-background environments with inert detection

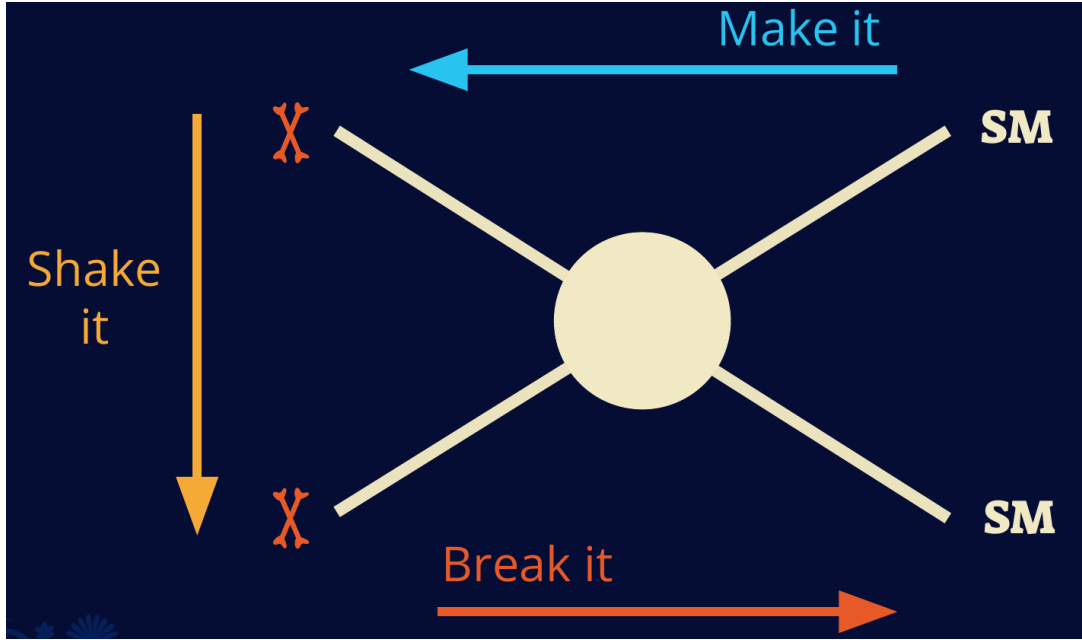


Figure 2.8 Simplified Feynman diagram demonstrating different ways DM can interact with SM particles. The 'X's refer to the DM particles whereas the SM refer to fundamental particles in the SM. The large circle in the center indicates the vertex of interaction and is purposely left vague. The colored arrows refer to different directions of time as well as their respective labels. The arrows indicate the initial and final state of the DM -SM interaction in time.

212 media like the noble gas Xenon. [14]

213 **Make it** refers to the production of DM from SM initial states. The experiment starts with
 214 particles in the SM. These SM particles are accelerated to incredibly high energies and then
 215 collide with each other. In the confluence of energy, DM hopefully emerges as a byproduct of the
 216 SM annihilation. Often it is the collider experiments that are energetic enough to hypothetically
 217 produce DM. These experiments include the world-wide collaborations ATLAS and CMS at CERN
 218 where proton collide together at extreme energies. The DM searches, however, are complex. DM
 219 likely does not interact with the detectors and lives long enough to escape the detection apparatus of
 220 CERN's colliders. This means any DM production experiment searches for an excess of events with
 221 missing momentum or energy in the events. An example event with missing transverse momentum
 222 is shown in ???. The missing momentum with no particle tracks implies a neutral particle carried
 223 the energy out of the detector. However, there are other neutral particles in the SM, like neutrons
 224 or neutrinos, so any analysis has to account for SM signatures of missing momentum. [15]

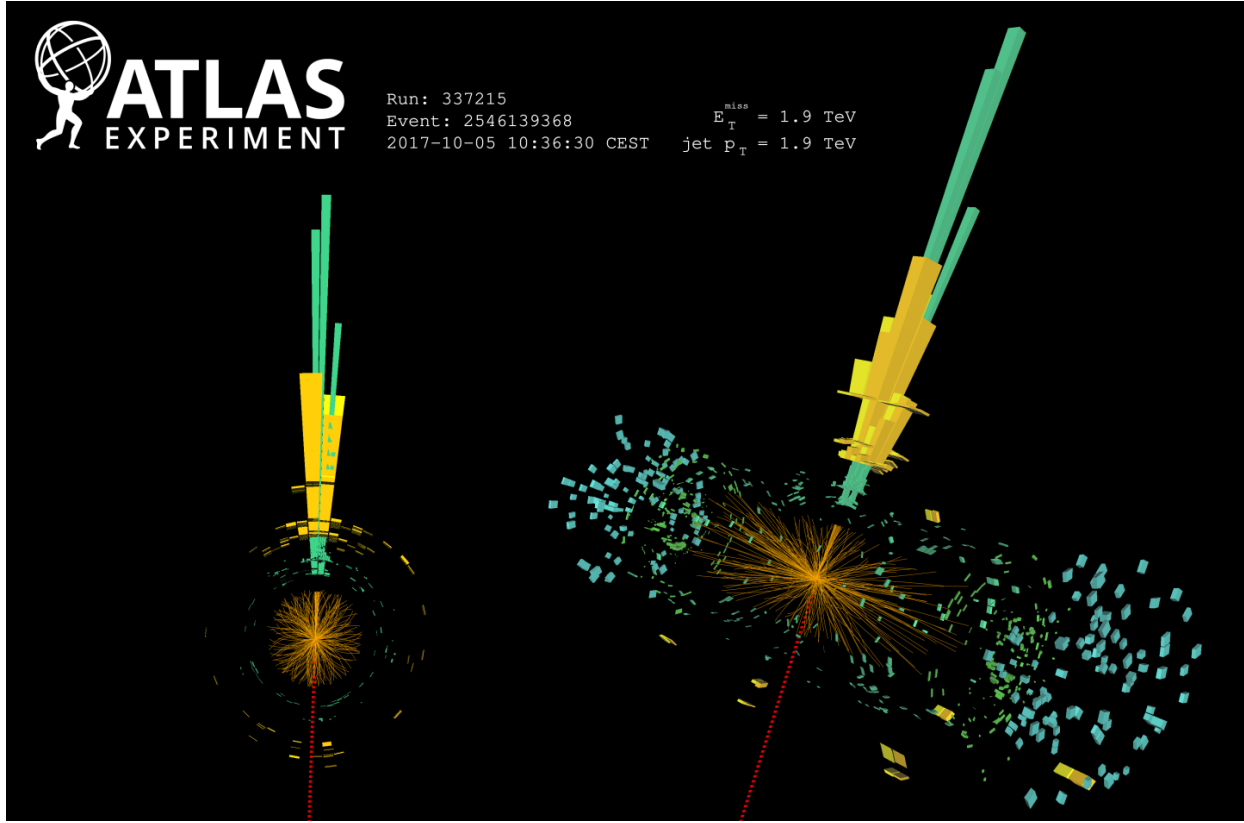


Figure 2.9 A single jet event in ATLAS detector from 2017 [16]. Jet momentum was observed to be 1.9 TeV. Missing transverse momentum was observed to be 1.9 TeV compared to the initial transverse momentum of the event was 0. Implied MET is traced by a red dashed line in event display.

225 2.4.2 Break it: Standard Model Signatures of Dark Matter through Indirect Searches

226 **Break it** refers to the creation of SM particles from the dark sector, and it is the primary focus

227 of this thesis. The interaction begins with DM or in the dark sector. The hypothesis is that this

228 DM will either annihilate with itself or decay and produce an SM byproduct. This method is

229 often referred to as the Indirect Detection of DM because we have no lab to directly control or

230 manipulate the DM. Therefore, most indirect DM searches are performed using observations of

231 known DM densities among the astrophysical sources. The strength is that we have the whole of the

232 universe and its 13.6-billion-year lifespan to use as a detector and particle accelerator. Additionally,

233 locations of dark matter are well cataloged since it was astrophysical observations that presented

234 the problem of DM in the first place.

235 However, anything can happen in the universe. There are many difficult to deconvolve back-

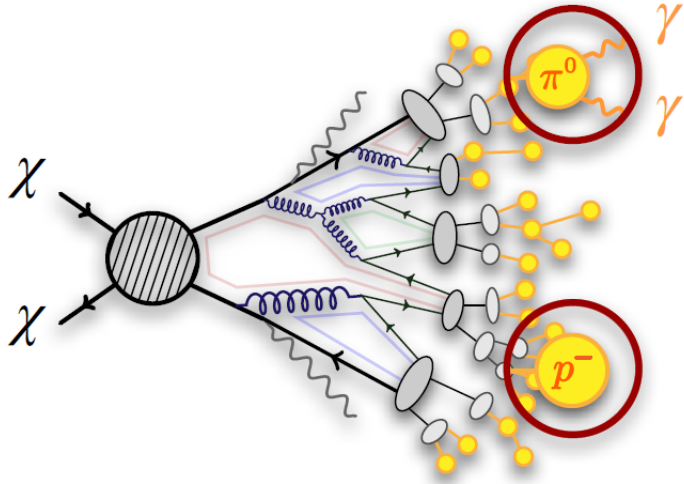


Figure 2.10 More detailed pseudo-Feynman diagram of particle cascade from dark matter annihilation into 2 quarks. The quarks hadronize and down to stable particles like γ or the anti-proton (p^-). Diagram pulled from ICRC 2021 presentation on DM annihilation search [17].

236 grounds when searching for DM. One prominent example is the galactic center. We know the
 237 galactic center has a large DM content because of stellar kinematics in our Milky Way and DM halo
 238 simulations. Yet, any signal from the galactic center is challenging to parse apart from the extreme
 239 environment of our supermassive black hole, unresolved sources, and diffuse emission from the
 240 interstellar medium [18]. Despite the challenges, any DM model that yields evidence in the other
 241 two observation methods, **Shake it or Make it** must be corroborated with indirect observations of
 242 the known DM sources. Without corroborating evidence, DM observation in the lab is hard-pressed
 243 to demonstrate that it is the model contributing to the DM seen at the universal scale.

244 In the case of WIMP DM, signals are described in terms of primary SM particles produced
 245 from DM decay or annihilation. The SM initial state particles are then simulated down to stable
 246 final states such as the γ , ν , p , or e which can traverse galactic lengths to reach Earth.

247 ?? shows the quagmire of SM particles that emerges from SM initial states that are not stable
 248 [17]. There are many SM particles with varying energies that can be produced in such an interaction.
 249 For any arbitrary DM source and stable SM particle, the SM flux from DM annihilating to a neutral

250 particle in the SM, ϕ , from a region in the sky is described by the following.

$$\frac{d\Phi_\phi}{dE_\phi} = \frac{\langle\sigma v\rangle}{8\pi m_\chi^2} \frac{dN_\phi}{dE_\phi} \times \int_{\text{source}} d\Omega \int_{l.o.s} \rho_\chi^2 dl(r, \theta') \quad (2.4)$$

251 n ??, $\langle\sigma v\rangle$ is the velocity-weighted annihilation cross-section of DM to the SM. m_χ refers to the
252 mass of DM, noted with Greek letter χ . $\frac{dN_\phi}{dE_\phi}$ is the N particle flux weighted by the particle energy.
253 An example is provided in ?? for the γ final state. The integrated terms are performed over the
254 solid angle, $d\Omega$, and line of sight, l.o.s. ρ is the density of DM for a location (r, θ') in the sky. The
255 terms left of the 'x' are often referred to as the particle physics component. The terms on the right
256 are referred to as the astrophysical component. For decaying DM, the equation changes to...

$$\frac{d\Phi_\phi}{dE_\phi} = \frac{1}{4\pi\tau m_\chi} \frac{dN_\phi}{dE_\phi} \times \int_{\text{source}} d\Omega \int_{l.o.s} \rho_\chi dl(r, \theta') \quad (2.5)$$

257 In ??, τ is the decay lifetime of the DM. Just as in ??, the left and right terms are the particle physics
258 and the astrophysical components respectively. The integrated astrophysical component of ?? is
259 often called the J-Factor. Whereas the integrated astrophysical component of ?? is often called the
260 D-Factor.

261 Exact DM $\text{DM} \rightarrow \text{SM}$ branching ratios are not known, so it is usually assumed to go 100%
262 into an SM particle/anti-particle. Additionally, when a DM annihilation or decay produces one of
263 the neutral, long-lived SM particles (ν or γ), the particle is traced back to a DM source. For DM
264 above GeV energies, there are very few SM processes that can produce particles with such a high
265 energy. Seeing such a signal would almost certainly be an indication of the presence of dark matter.
266 Fortunately, the universe provides us with the largest volume and lifetime ever for a particle physics
267 experiment.

268 **2.5 Sources for Indirect Dark Matter Searches**

269 The first detection of DM relied on optical observations. Since then, we have developed new
270 techniques to find DM dense regions. As described in ??, many DM dense regions were through
271 observing galactic rotation curves. Our Milky Way galaxy is among DM dense regions discovered,
272 and it is the largest nearby DM dense region to look at. Additionally, the DM halo surrounding the
273 Milky Way is clumpy [18]. There are regions in the DM halo of the Milky Way that have more DM

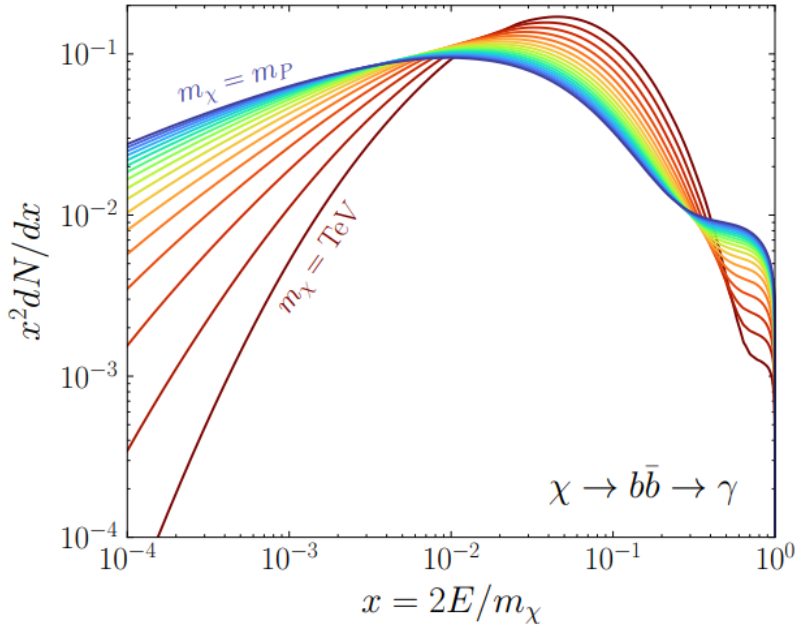


Figure 2.11 Dark Matter (DM) decay spectrum for $b\bar{b}$ initial state and γ final state. Redder spectra are for larger DM masses. Bluer spectra are light DM masses. x is a unitless factor defined as the ratio of the mass of DM, m_χ , and the final state particle energy E_γ . Figure from [19].

than others that have captured gas over time. These sub-halos were dense enough collapse gas and form stars. These apparent sub galaxies are known as dwarf spheroidal galaxies and are the main sources studied in this thesis. Each source type comes with different trade-offs. Galactic Center studies will be very sensitive to the assumed distribution of DM. The central DM density can vary substantially as demonstrated in ???. At distances close to the center of the galaxy, or small r , the differences in DM densities can be 3-4 orders of magnitude. Searches toward the galactic center will therefore be quite sensitive to the assumed DM distribution.

Searches toward Dwarf Spheroidal Galaxies (dSph's) suffer from uncertainties in the DM density less than the galactic center studies. This is mostly from their diminutive size being smaller than the angular resolution of most γ -ray observatories [18]. The DM content dSph's are typically determined with the Virial theorem, ???, and are usually majority DM [18] in mass. Dsph's tend to be ideal sources to look at for DM searches. Their environments are quiet with little astrophysical background. Unlike the galactic center, the most active components of dSph's are the stars within them versus a violent accretion disc around a black hole. All this together means that dSph's are

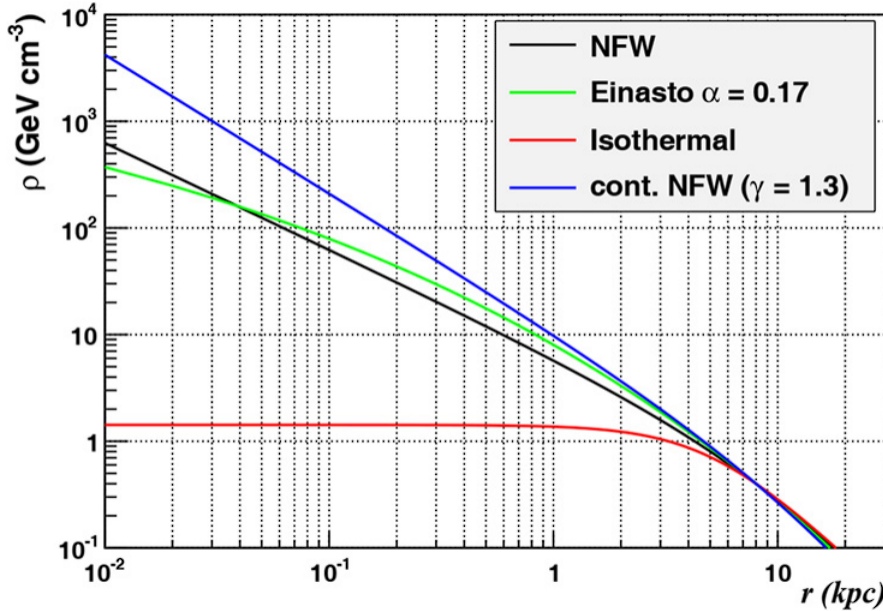


Figure 2.12 Different dark matter density profiles compared. Some models produce exceptionally large densities at small r [20].

288 among the best sources to look at for indirect DM searches. dSph's are the targets of focus for this
 289 thesis.

290 2.6 Multi-Messenger Dark Matter

291 Astrophysics entered a new phase in the past few decades that leverages our increasing sensitivity
 292 to SM channels and general relativity (GR). Up until the 21st century, astrophysical observations
 293 were performed with photons (γ) only. Astrophysics with this 'messenger' is fairly mature now.
 294 Novel observations of the universe have since only adjusted the sensitivity of the wavelength of
 295 light that is observed except at MeV energies. Gems like the CMB [10], and more have ultimately
 296 been observations of different wavelengths of light. Multi-messenger astrophysics proposes using
 297 other SM particles such the $p^{+/-}$, or ν or gravitation waves predicted by general relativity.

298 The experiment LIGO had a revolutionary discovery in 2016 with the first detection of a binary
 299 black hole merger [21]. This opened the collective imagination to observing the universe through
 300 gravitational waves. There has also been a surge of interest in the neutrino (ν) sector. IceCube
 301 demonstrated that we are sensitive to neutrinos in regions that correlate with significant photon
 302 emission like the galactic plane [22]. Neutrinos, like gravitational waves and light, travel mostly

303 unimpeded from their source to our observatories. This makes pointing to the originating source
 304 of these messengers much easier than it is for cosmic rays which are deflected from their source by
 305 magnetic fields.

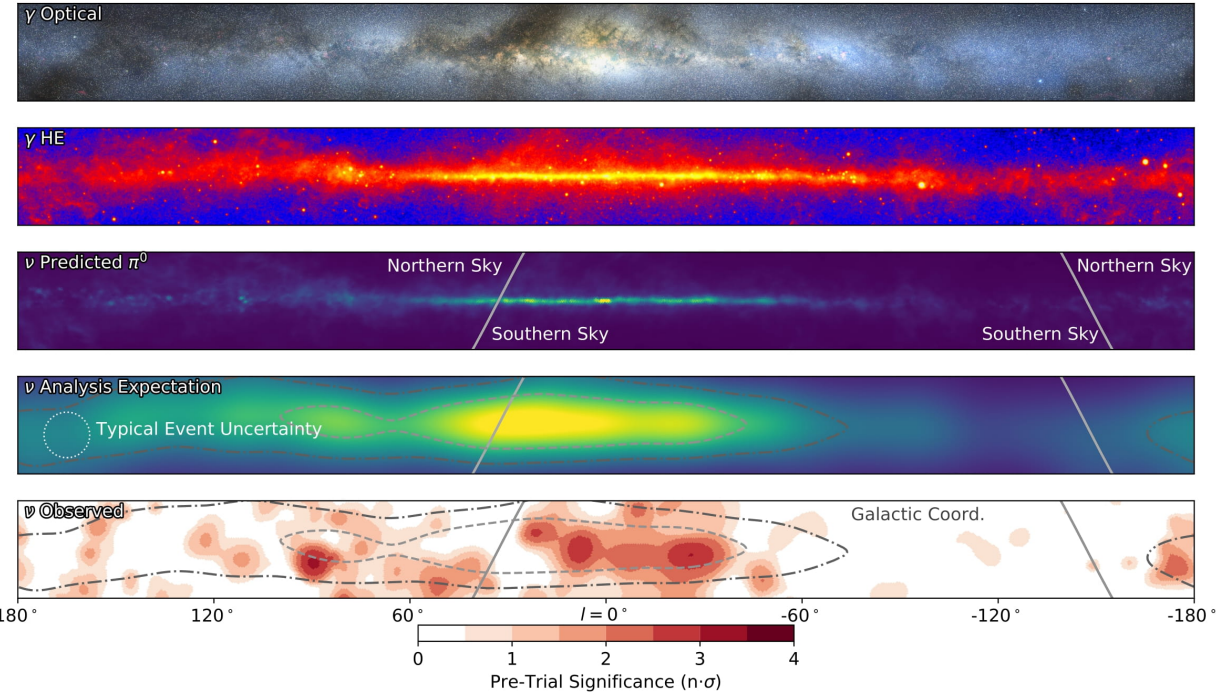


Figure 2.13 The Milky Way Galaxy in photons (γ) and neutrinos (ν) [22]. The Galactic center is at $l=0^\circ$ and is the brightest region in all panels. (top) An Optical color image of the Milky Way galaxy seen from Earth. Clouds of gas and dust obscure some light from stars. (2nd down) Integrated flux of γ -rays observed by the Fermi-LAT telescope [23]. (middle) Expected neutrino emission that corresponds with Fermi-LAT observations. (2nd up) Expected neutrino emission profile after considering detector systematics of IceCube. (bottom) Observed neutrino emission from region of the galactic plane. Substantial neutrino emission was detected.

306 The IceCube collaboration recently published a groundbreaking result of the Milky Way in
 307 neutrinos. The recent result from IceCube, shown in ??, proves that we can make observations
 308 under different messenger regimes. The top two panels show the appearance of the galactic plane
 309 to different wavelengths of light. Some sources are more apparent in some panels, while others are
 310 not. This new channel is powerful because neutrinos are readily able to penetrate through gas and
 311 dust in the Milky Way. This new image also refines our understanding of how high energy particles
 312 are produced. For example, the fit to IceCube data prefers neutrino production from the decay of
 313 π^0 [22].

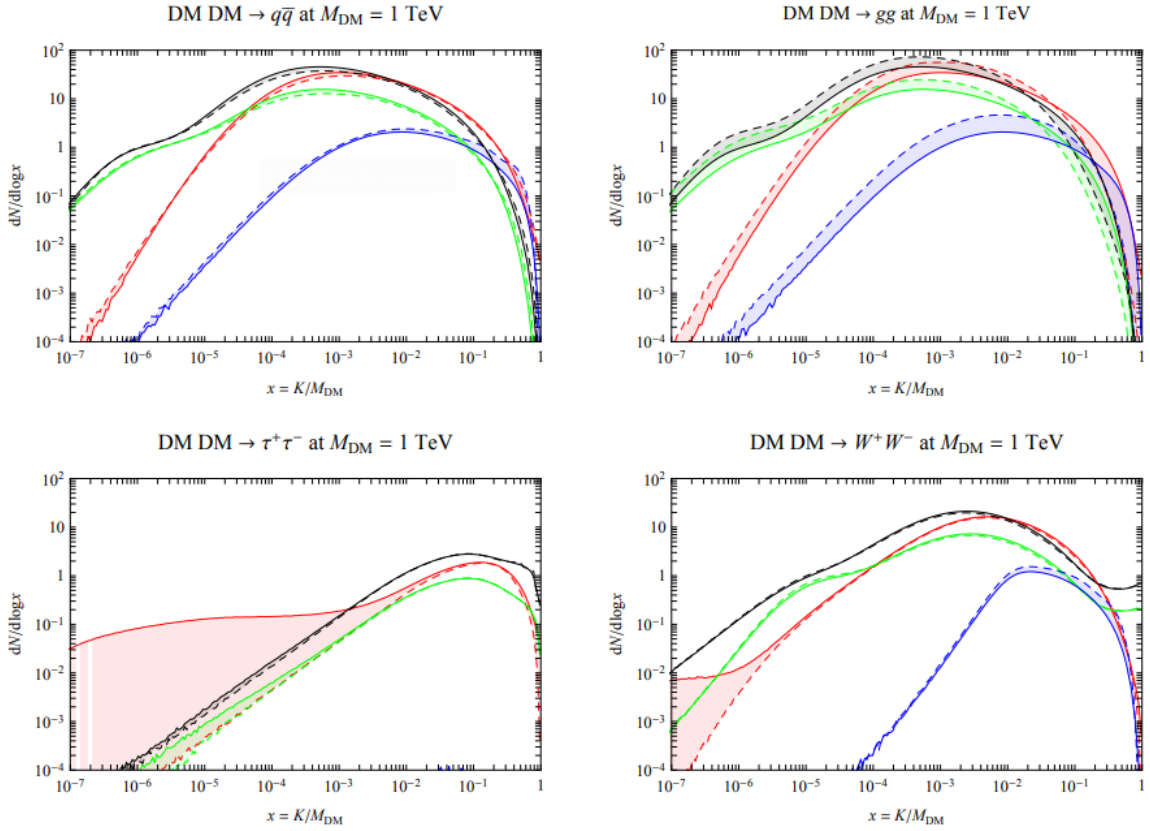


Figure 2.14 Dark Matter annihilation spectra for different final state particle and standard model annihilation channels [24]. Photons (red), e^\pm (green), \bar{p} (blue), ν (black).

314 Exposing our observations to more cosmic messengers greatly increases our sensitivity to rare
 315 processes. In the case of DM, ??, there are many SM particles produced in DM annihilation.
 316 Among the final state fluxes are gammas and neutrinos. Charged particles are also produced
 317 however they would not likely make it to Earth since they will be deflected by magnetic fields
 318 between the source and Earth. This means observatories that can see the neutral messengers are
 319 especially good for DM searches and for combining data for a multi-messenger DM search.

CHAPTER 3

320 MULTIMESSENGER ASTROPHYSICS: DETECTING HIGH ENERGY NEUTRAL 321 MESSENGERS

322 3.1 Introduction

323 Before the 20th century, all astrophysics observations were optical in nature. We literally only
324 saw things with highly magnified optical observations. Then we discovered cosmic rays. cosmic
325 rays are charged particles, typically naked protons or H+. This was seen by Victor Hess in 19??.
326 Around the same time we discovered neutrinos from beta decay. Sometime around 1950 we started
327 to build neutrino detectors which were mostly sensitive to neutrinos from the sun. Finally, it was
328 theorized that compact objects like black holes and neutron stars would create waves in space-time
329 when they experience mergers or collisions.

330 In the 21st century, we have developed new observation techniques and detectors that are no only
331 sensitive to these four messengers - photons ([TODO: photon](#)), neutrinos ([TODO: nu](#)), Cosmic
332 Rays (CR), and Gravitational Wave (WV) - we're collect high energy versions of these events.
333 For the standad model particles, we're now sensitive to all messengers above the MeV eneryg
334 range. Additionally, the GW's were sensitive to are in the stellar mass black hole region and above
335 within our galactic neighborhood. This means were becoming sensitive to the fundamental physics
336 occuring within the universe and we can rely on the universe as a TeV+ particle accelerator. We
337 also have the abaility to correlate high energy events across messengers and gain new insights on
338 the processes that occur in our universe.

339 This thesis focuses on very high energy (VHE) gamma rays and neutrinos. These can both be
340 observed through the water cherenkov detection technique altho not exclusively. Methods on how
341 to detect and observe these neutral messengers are discussed ?? and ??

342 3.2 Charged Particles in a Medium

343 For high enery gamma-rays and neutrinos, we can exploit the same effect that charged particles
344 have with water. This effect is known as Cherenkov radiation. Cherenkov Radiation occurs when a
345 charged particle, usually electrons (e) or muons (μ), traverse a medium, like water, faster than the

346 speed of light in that medium. This is similar to sonic boom where an object moves through air
347 faster than the speed of sound in air. Cherenkov radiation can therefore be thought of as an 'optic
348 boom'. Many astro-particle physics experiments will use water as the medium as because water
349 has a unique set of properties ideal for charged particle tracking.



Figure 3.1 TODO: Show a nuclear reactor with cherenkov radiation[NEEDS A SOURCE][FACT CHECK THIS]

350 The frequency of light emitted due to cherenkov radiation follows the equation:

$$INSERT\ Cherenkov\ wavelength\ calc\ HERE. \quad (3.1)$$

351 The absorption spectra is shown in the following figure:

352 **3.3 Photons (γ)**

353 **3.4 Neutrinos (ν)**

354 **3.5 Opportunities to Combine for Dark Matter**



Figure 3.2 TODO: absorption spectrum of liquid and solid water[NEEDS A SOURCE][FACT CHECK THIS]

CHAPTER 4

355

HIGH ALTITUDE WATER CHERENKOV (HAWC) OBSERVATORY

356 **4.1 The Detector**

357 **4.2 Events Reconstruction and Data Acquisition**

358 **4.2.1 G/H Discrimination**

359 **4.2.2 Angle**

360 **4.2.3 Energy**

361 **4.3 Remote Monitoring**

362 **4.3.1 ATHENA Database**

363 **4.3.2 HOMER**

364

CHAPTER 5

ICECUBE NEUTRINO OBSERVATORY

365 **5.1 The Detector**

366 **5.2 Events Reconstruction and Data Acquisition**

367 **5.2.1 Angle**

368 **5.2.2 Energy**

369 **5.3 Northern Test Site**

370 **5.3.1 PIgeon remote dark rate testing**

371 **5.3.2 Bulkhead Construction**

CHAPTER 6

COMPUTATIONAL TECHNIQUES IN PARTICLE ASTROPHYSICS

373 **6.1 Neural Networks for Gamma/Hadron Separation**

374 **6.2 Parallel Computing for Dark Matter Analyses**

CHAPTER 7

GLORY DUCK: MULTI-WAVELENGTH SEARCH FOR DARK MATTER ANNIHILATION TOWARDS DWARF SPHEROIDAL GALAXIES

377 7.1 Introduction

378 The field of astrophysics now has several instruments and observatories sensitive to high energy
 379 gamma-rays. The energy sensitivity for the modern gamma-ray program spans many orders of
 380 magnitude. ?? demonstrates these similar sensitivities across energies for the five experiments:
 381 Fermi-LAT, HAWC, HESS, MAGIC, and VERITAS.

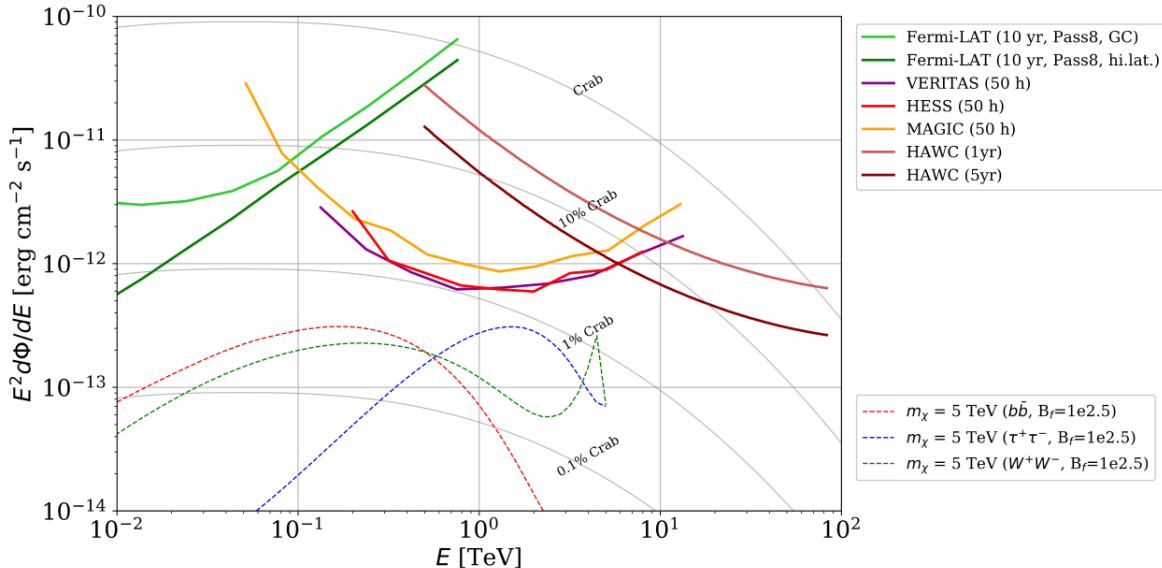


Figure 7.1 [NEEDS A SOURCE] Sensitivities of five gamma-ray experiments compared to percentages of the Crab nebula's emission and dark matter annihilation. Solid lines present estimated sensitivities to power law spectra [FACT CHECK THIS] for each experiment. Green lines are Fermi-LAT sensitivities where lighter green is the sensitivity to the galactic center and light green is its sensitivity to higher declinations. Orange, red, and purple solid lines represent the MAGIC, HESS, and VERITAS 50 hour sensitivities respectively. The maroon and brown lines are the HAWC 1 year and 5 year sensitivities. Across four decades of gamma-ray energy, these experiments have similar sensitivities on the order 10^{-12} erg cm $^{-2}$ s $^{-1}$. The dotted lines are estimated dark matter fluxes assuming DM annihilating to bottom quarks (red), tau leptons (blue), and W bosons (green). Faded grey lines outline percentage flux of the Crab nebula.

382 Each of the five experiments featured in ?? have independently searched for DM annihilation
 383 from dwarf galaxies and set limits. Intriguingly, their similarities overlap in regions where these
 384 observatories are less sensitive. This clearly motivates an analysis that combines data from these

385 five. Each experiment has unique gamma-ray detection methods and their weaknesses and
386 strengths can be leveraged with each other. The HAWC gamma-ray observatory is extensively
387 introduced in ??, so it is not introduced here. A brief description of the remaining experiments are
388 in the following paragraphs.

389 The Large Area Telescope (LAT) is a pair conversion telescope mounted on the NASA Fermi
390 satellite in orbit 550 km above the Earth [25]. LAT's field of view covers about 20% of the
391 whole sky, and it sweeps the whole sky every 3 hours, approximately. LAT's gamma-ray energy
392 sensitivity ranges from 20 MeV up to 1 TeV. Previous DM searches towards dwarf galaxies using
393 Fermi-LAT are published in [26] and [27]

394 The High Energy Spectroscopic System (HESS), Major Atmospheric Gamma Imaging
395 Cherenkov (MAGIC), and Very Energetic Radiation Imaging Telescope Array System (VERI-
396 TAS) are arrays of Imaging Atmospheric Cherenkov Telescopes (IACT). These telescopes observe
397 the Cherenkov light emmited from gamma-ray showers in the Earth's atmosphere. The field for
398 these telescopes is no larger than 5° with energy sensitivities ranging from 30 GeV up to 100 TeV.
399 [28, 29, 30] IACTs are able to make precise observations in selected regions of the sky, however
400 can only be operated in ideal dark conditions. HESS's observations of the dwarves Sculptor and
401 Carina were between January 2008 and December 2009. HESS observations of Coma Berenices
402 were from 2010 to 2013, and Fornax was observed in 2010 [31, 32, 33]. MAGIC provided deep
403 observations of Segue1 between 2011 and 2013 [34]. MAGIC also provides data for three dwarves:
404 Coma Berenices, Draco, and Ursa Major II where observations were made in: January - June 2019
405 [35], March - September 2018 [35], and 2014 - 2016 [36] respectively. VERITAS provided data
406 for Boötes I, Draco, Segue 1, and Ursa Minor from 2009 to 2016 [37]

407 This chapter presents the Glory Duck analysis, the name given for the search for dark matter
408 annihilation from dwarf galaxies by combining data from the five gamma-ray observatories: Fermi-
409 LAT, HAWC, HESS, MAGIC, and VERITAS. Specifically, the methods in analysis and modeling
410 are presented for the HAWC gamma-ray observatory. This work was published to ??? and presented
411 at the International Cosmic Ray Conference in 2019, 2021, and 2023 [38, 39, 40] and more.

412 **7.2 Dataset and Background**

413 This section enumerates the data and background methods used for HAWC's study of the dwarf
414 spheroidal galaxies (dSph). ?? and ?? are most useful for fellow HAWC collaborators looking to
415 replicate the Glory Duck analysys.

416 **7.2.1 Itemized HAWC files**

- 417 • Detector Resolution: [response_aerie_svn_27754_systematics_best_mc_test_no](#)
418 [broadpulse_10pctlogchargesmearing_0.63qe_25kHzNoise_run5481_curvatu](#)
419 [re0_index3.root](#)
- 420 • Data Map: [maps-20180119/liff/maptree_1024.root](#)
- 421 • Spectral Dictionary: [DM_CirrelliSpectrum_dict_gammas.npy](#)
- 422 • Analysis wiki: https://private.hawc-observatory.org/wiki/index.php/Glory_Duck_Multi-Experiment_Dark_Matter_Search

424 **7.2.2 Software Tools and Development**

425 This analysis was performed using HAL and 3ML, in Python version 2[41, 42]. I built software
426 to implement the *Poor Particle Physicists' Cookbook* (PPPC) [43] DM spectral model and dSphs
427 spatial model from [44] for HAWC analysis. A NumPy version of this dictionary was made for
428 both Py2 and Py3. The code base for creating this dictionary is linked on my GitLab sandbox:

- 429 • Py2: [Dictionary Generator \(Deprecated\)](#)
- 430 • Py3: [PPPC2Dict](#)

431 The analysis was performed using the f_{hit} framework performed in the Crab paper[41]. The
432 Python2 NumPy dictionary file for gamma-ray final states is [dmCirSpecDict.npy](#). The corre-
433 sponding Python3 file is [DM_CirrelliSpectrum_dict_gammas.npy](#). These files can also be
434 used for decay channels and the PPPC describes how. [43]. All other software used for data

435 analysis, DM profile generation, and job submission to SLURM are also kept in my sandbox for
436 the [Glory Duck](#) project.

437 **7.2.3 Data Set and Background Description**

438 The HAWC data maps used for this analysis contain 1017 days of data between runs 2104
439 (2014-11-26) and 7476 (2017-12-20). They were generated from pass 4.0 reconstruction. The
440 analysis is performed using the f_{hit} energy binning scheme with bins (1-9) similar to what was done
441 for the Crab and previous HAWC dSph analysis. [41, 45]. Bin 0 was excluded as it has substantial
442 hadronic contamination and poor angular resolution.

443 This analysis was done on dwarf spheroidal (dSph) galaxies because of their large dark matter
444 (DM) content relative to baryonic. We consider the following to estimate the background to this
445 study.

- 446 • The dSphs are small in HAWC’s field of view, so the analysis is not sensitive to large or small
447 scale anisotropies.
- 448 • The dSphs used in this analysis are off the galactic plane.
- 449 • The dSphs are baryonically faint relative to their expected dark matter content and are not
450 expected to contain gamma-ray sources.

451 Therefor we make no additional assumptions on the background from our sources and use
452 HAWC’s standard direct integration method for background estimation [41]. It is possible for
453 gamma rays from DM annihilation to scatter in transit to HAWC via Inverse Compton Scattering
454 (ICS). This was investigated and its impact on the flux is basically zero. Supporting information
455 on this is in ??

456 **7.3 Analysis**

457 The expected differential photon flux from DM-DM annihilation to standard model particles
458 over solid angle is described by the familiar equation.

$$\frac{d\Phi_\gamma}{dE_\gamma} = \frac{\langle\sigma v\rangle}{8\pi m_\chi^2} \frac{dN_\gamma}{dE_\gamma} \times \int_{\text{source}} d\Omega \int_{l.o.s} \rho_\chi^2 dl(r, \theta') \quad (7.1)$$

459 Where $\langle \sigma v \rangle$ is the velocity weighted annihilation cross-section. $\frac{dN}{dE}$ is the expected differential
 460 number of photons produced at each energy per annihilation. M_χ is the rest mass of the supposed
 461 DM particle. J is the astrophysical J-factor and is defined as

$$J = \int \int \rho_\chi^2(l, \Omega) dl d\Omega \quad (7.2)$$

462 ρ_χ is the DM density. How each component is generated and considered for HAWC's analysis
 463 is presented in the following sections.

464 **7.3.1 $\frac{dN_\gamma}{dE_\gamma}$ - Particle Physics Component**

465 For this value, we import the PPPC with Electro-Weak (EW) corrections [43]. The spectrum is
 466 implemented as a model script in astromodels for 3ML. The PPPC model selected for this analysis
 467 included EW corrections. The EW corrections were previously not considered for HAWC and are
 468 significant for DM annihilating to EW coupled SM particles such as all leptons, and the γ , Z , and
 469 W bosons. [45]. ?? demonstrates the significance of EW corrections for W boson annihilation.
 470 Tables from the PPPC were reformatted into python Numpy dictionaries for collaboration-wide
 471 use. A class in astromodels was created to include the EW correction from the PPPC and is aptly
 472 named PPPCSpectra within `DM_models.py`.

473 **7.3.2 J - Astrophysical Component**

474 The J-factor profiles for each source are imported from Geringer-Sameth (GS) [44]. These
 475 were provided from the authors as $J(\theta)$, where θ is the angular separation from the center of the
 476 source. HAWC requires maps in terms of $\frac{dJ}{d\Omega}$, so the conversion from the maps was done in the
 477 following way.

478 First, convert the angular distances to solid angles

$$\Omega = 2 \cdot \pi(1 - \cos(\theta)) \quad (7.3)$$

479 which reduces with a small angle approximation to $\pi\theta^2$. Next, the central difference for both the ΔJ
 480 and $\Delta\theta$ value were calculated for the discretized form of $J(\theta)$ with the central difference stencil:

$$\Delta\phi_i = \phi_{i+1} - \phi_{i-1} \quad (7.4)$$

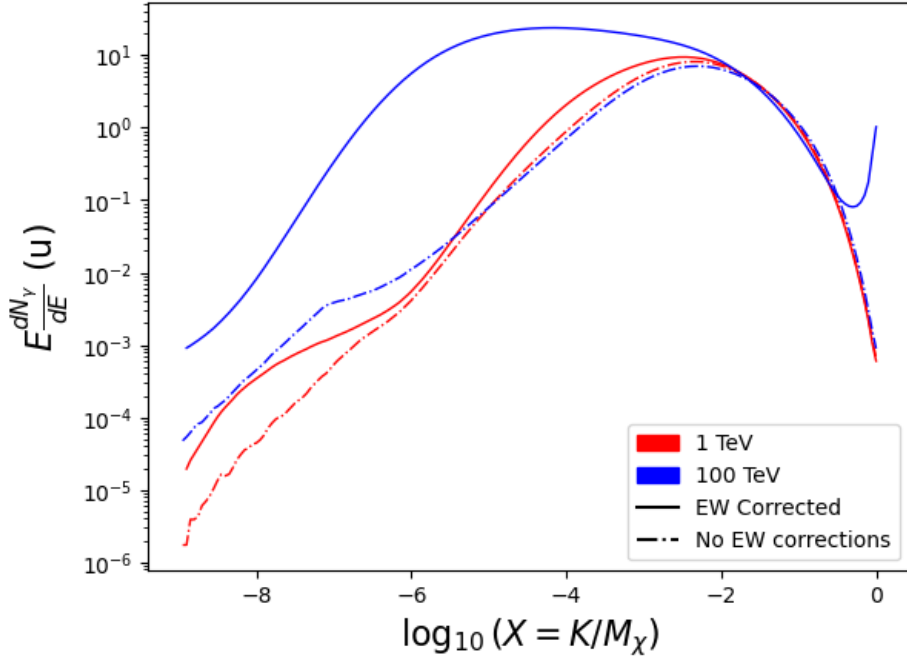


Figure 7.2 Effect of Electro-Weak (EW) corrections on expected DM annihilation spectrum for $\chi\chi \rightarrow W^-W^+$. Solid lines are spectral models that consider EW corrections. Dash-dot lines are spectral models without EW corrections. Red lines are models for $M_\chi = 1$ TeV. Blue lines represent models for $M_\chi = 100$ TeV. All models are sourced from the PPPC4DMID [43].

481 Where ϕ is either θ or J . These were done separately in case the grid spacing in θ was not uniform.
 482 Finally, these lists are divided so that we are left with approximation of the profile of $dJ/d\Omega$ that
 483 is a function of θ . Admittedly, this is an approximation method for the map which introduces
 484 small errors compared to the true profile estimate. This was checked as a systematic against the
 485 author's profiling of the spatial distribution and is documented in **TODO: Model dependant limit,**
 486 **remember the jfactors!**

487 With $\frac{dJ}{d\Omega}$, a map is generated, first by filling in the north-east quadrant of the map. This quadrant
 488 is then reflected twice, vertically then horizontally, to fill the full map. Maps are then normalized
 489 by dividing the discrete 2D integral of the map. The 2D integral was a simple height of bins,
 490 Newton's integral:

$$p^2 \cdot \sum_{i,j=0}^{N,M} \frac{dJ}{d\Omega}(\theta_{i,j}) \quad (7.5)$$

491 These maps are HEALpix maps with NSIDE 16384 and saved in the `.fits` format.
 492 Another DM spatial distribution model from Bonnivard (\mathcal{B}) [46] was used for the complete

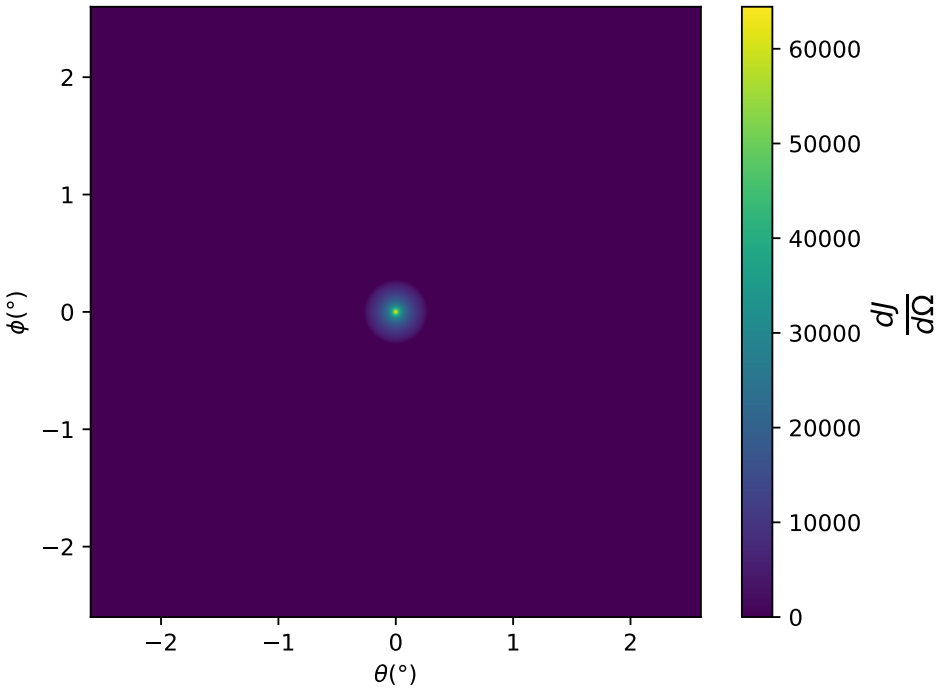
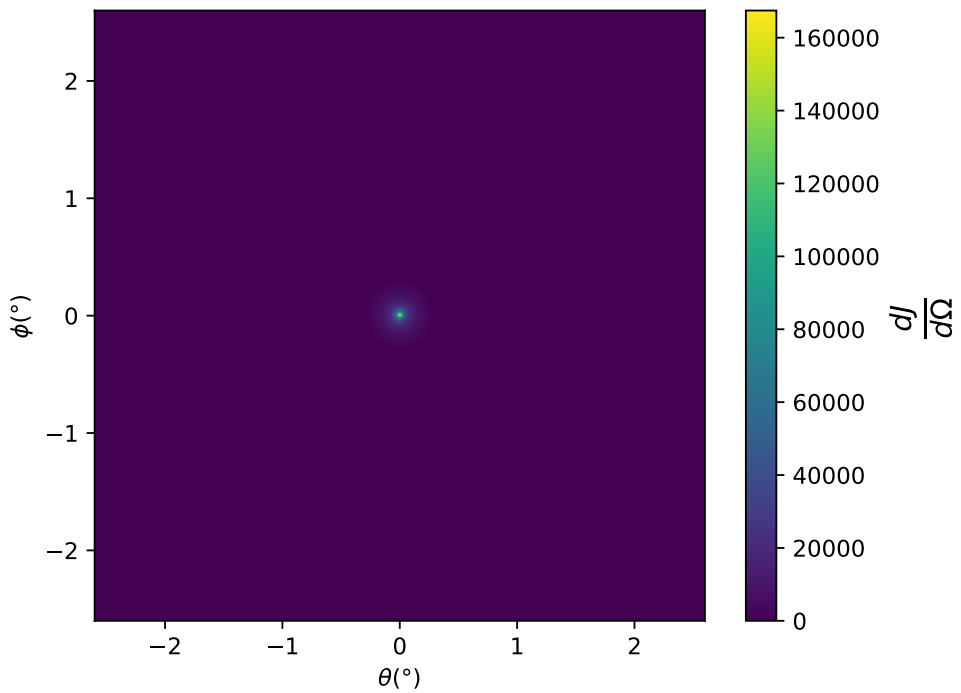


Figure 7.3 $\frac{dJ}{d\Omega}$ maps for Segue1 (top) and Coma Berenices (bottom). Origin is centered on the specific dwarf spheroidal galaxies (dSph). X and Y axes are the angular separation from the center of the dwarf. Plots of the remaining 11 dSph HAWC studied are linked in ??.

study. However, to save computational time, limits from \mathcal{GS} were scaled to \mathcal{B} instead of each experiment performing a full study a second time. How these models compare is demonstrated for each dSph in ?? and ?? Plots of these maps are provided for each source in the sandbox directory: `GD_mass_profiles`. Examples of the two most impactful dSphs, Segue1 and Coma Berenices are featured in ??

7.3.3 Source Selection and Annihilation Channels

We use many of the dSph presented in our previous dSph DM search [45]. HAWC's sources for Glory Duck include Boötes I, Coma Berenices, Canes Venatici I + II, Draco, Hercules, Leo I, II, + IV, Segue 1, Sextans, and Ursa Major I + II. A full description of all sources used in Glory Duck is found in ?. Triangulum II was excluded from the Glory Duck analysis because of large uncertainties in its J-factor. Ursa Minor was excluded from HAWC's contribution to the combination because the source extension model extended Ursa Minor beyond HAWC's field of view. Ursa Minor was not expected to contribute significantly to the combined limit, so work was not invested in a solution to include Ursa Minor.

The DM annihilation channels probed for the Glory Duck combination include $b\bar{b}$, $e\bar{e}$, $\mu\bar{\mu}$, $\tau\bar{\tau}$, $t\bar{t}$, W^+W^- , and ZZ . A summary of all sources, with a description of each experiments' sensitivity to the source, is provided in ??.

7.3.4 Likelihood Methods

We perform a standard HAWC binned maximum likelihood analysis using f_{hit} bins 1-9. This analysis was performed using HAL and 3ML, in Python2 [41, 42]. With these tools we compute the max from the likelihood profiles and perform a ratio test to calculate the significance of each source. This analysis is identical to the previous dSph analysis [45] except the sources are treated as extended. For the vast majority of our sources, this extension is no greater than 2 degrees. We calculate the likelihood of each source and model, assuming events are Poisson distributed, with

$$\mathcal{L} = \prod_i \frac{(B_i + S_i)^{N_i} e^{-(B_i + S_i)}}{N_i!} \quad (7.6)$$

S_i is the sum of expected number of signal counts. B_i is the number of background counts

Table 7.1 Summary of the relevant properties of the dSphs used in the present work. Column 1 lists the dSphs. Columns 2 and 3 present their heliocentric distance and galactic coordinates, respectively. Columns 4 and 5 report the J -factors of each source given from the \mathcal{GS} and \mathcal{B} independent studies and their estimated $\pm 1\sigma$ uncertainties. The values $\log_{10} J$ (\mathcal{GS} set) [44] correspond to the mean J -factor values for a source extension truncated at the outermost observed star. The values $\log_{10} J$ (\mathcal{B} set) [46] are provided for a source extension at the tidal radius of each dSph. **Bolded sources are within HAWC's field of view and provided to the Glory Duck analysis.**

Name	Distance (kpc)	l, b ($^{\circ}$)	$\log_{10} J$ (\mathcal{GS} set) $\log_{10}(\text{GeV}^2\text{cm}^{-5}\text{sr})$	$\log_{10} J$ (\mathcal{B} set) $\log_{10}(\text{GeV}^2\text{cm}^{-5}\text{sr})$
Boötes I	66	358.08, 69.62	$18.24^{+0.40}_{-0.37}$	$18.85^{+1.10}_{-0.61}$
Canes Venatici I	218	74.31, 79.82	$17.44^{+0.37}_{-0.28}$	$17.63^{+0.50}_{-0.20}$
Canes Venatici II	160	113.58, 82.70	$17.65^{+0.45}_{-0.43}$	$18.67^{+1.54}_{-0.97}$
Carina	105	260.11, -22.22	$17.92^{+0.19}_{-0.11}$	$18.02^{+0.36}_{-0.15}$
Coma Berenices	44	241.89, 83.61	$19.02^{+0.37}_{-0.41}$	$20.13^{+1.56}_{-1.08}$
Draco	76	86.37, 34.72	$19.05^{+0.22}_{-0.21}$	$19.42^{+0.92}_{-0.47}$
Fornax	147	237.10, -65.65	$17.84^{+0.11}_{-0.06}$	$17.85^{+0.11}_{-0.08}$
Hercules	132	28.73, 36.87	$16.86^{+0.74}_{-0.68}$	$17.70^{+1.08}_{-0.73}$
Leo I	254	225.99, 49.11	$17.84^{+0.20}_{-0.16}$	$17.93^{+0.65}_{-0.25}$
Leo II	233	220.17, 67.23	$17.97^{+0.20}_{-0.18}$	$18.11^{+0.71}_{-0.25}$
Leo IV	154	265.44, 56.51	$16.32^{+1.06}_{-1.70}$	$16.36^{+1.44}_{-1.65}$
Leo V	178	261.86, 58.54	$16.37^{+0.94}_{-0.87}$	$16.30^{+1.33}_{-1.16}$
Leo T	417	214.85, 43.66	$17.11^{+0.44}_{-0.39}$	$17.67^{+1.01}_{-0.56}$
Sculptor	86	287.53, -83.16	$18.57^{+0.07}_{-0.05}$	$18.63^{+0.14}_{-0.08}$
Segue I	23	220.48, 50.43	$19.36^{+0.32}_{-0.35}$	$17.52^{+2.54}_{-2.65}$
Segue II	35	149.43, -38.14	$16.21^{+1.06}_{-0.98}$	$19.50^{+1.82}_{-1.48}$
Sextans	86	243.50, 42.27	$17.92^{+0.35}_{-0.29}$	$18.04^{+0.50}_{-0.28}$
Ursa Major I	97	159.43, 54.41	$17.87^{+0.56}_{-0.33}$	$18.84^{+0.97}_{-0.43}$
Ursa Major II	32	152.46, 37.44	$19.42^{+0.44}_{-0.42}$	$20.60^{+1.46}_{-0.95}$
Ursa Minor	76	104.97, 44.80	$18.95^{+0.26}_{-0.18}$	$19.08^{+0.21}_{-0.13}$

Table 7.2 Summary of dSph observations by each experiment used in this work. A ‘-’ indicates the experiment did not observe the dSph for this study. For Fermi-LAT, the exposure at 1 GeV is given. For HAWC, $|\Delta\theta|$ is the absolute difference between the source declination and HAWC latitude. HAWC is more sensitive to sources with smaller $|\Delta\theta|$. For IACTs, we show the zenith angle range, the total exposure, the energy range, the angular radius θ of the signal or ON region, the ratio of exposures between the background-control (OFF) and signal (ON) regions (τ), and the significance of gamma-ray excess in standard deviations, σ .

Source name	Fermi-LAT	HAWC	H.E.S.S, MAGIC, VERITAS						
	Exposure (10^{11} s m 2)	$ \Delta\theta $ (°)	IACT	Zenith (°)	Exposure (h)	Energy range (GeV)	θ (°)	τ	S (σ)
Boötes I	2.6	4.5	VERITAS	15 – 30	14.0	100–41000	0.10	8.6	-1.0
Canes Venatici I	2.9	14.6	–	–	–	–	–	–	–
Canes Venatici II	2.9	15.3	–	–	–	–	–	–	–
Carina	3.1	–	H.E.S.S.	27 – 46	23.7	310 – 70000	0.10	18.0	-0.3
Coma Berenices	2.7	4.9	H.E.S.S.	47 – 49	11.4	550 – 70000	0.10	14.4	-0.4
Draco	3.8	38.1	MAGIC	5 – 37	49.5	60 – 10000	0.17	1.0	–
			MAGIC	29 – 45	52.1	70 – 10000	0.22	1.0	–
			VERITAS	25 – 40	49.8	120 – 70000	0.10	9.0	-1.0
Fornax	2.7	–	H.E.S.S.	11 – 25	6.8	230 – 70000	0.10	45.5	-1.5
Hercules	2.8	6.3	–	–	–	–	–	–	–
Leo I	2.5	6.7	–	–	–	–	–	–	–
Leo II	2.6	3.1	–	–	–	–	–	–	–
Leo IV	2.4	19.5	–	–	–	–	–	–	–
Leo V	2.4	–	–	–	–	–	–	–	–
Leo T	2.6	–	–	–	–	–	–	–	–
Sculptor	2.7	–	H.E.S.S.	10 – 46	11.8	200 – 70000	0.10	19.8	-2.2
Segue I	2.5	2.9	MAGIC	13 – 37	158.0	60 – 10000	0.12	1.0	-0.5
			VERITAS	15 – 35	92.0	80 – 50000	0.10	7.6	0.7
Segue II	2.7	–	–	–	–	–	–	–	–
Sextans	2.4	20.6	–	–	–	–	–	–	–
Ursa Major I	3.4	32.9	–	–	–	–	–	–	–
Ursa Major II	4.0	44.1	MAGIC	35 – 45	94.8	120 – 10000	0.30	1.0	-2.1
Ursa Minor	4.1	–	VERITAS	35 – 45	60.4	160 – 93000	0.10	8.4	-0.1

518 observed. N_i is the total number of counts. The i th bin is iterated over spatial and f_{hit} . Then we
 519 combine the profiles across all five experiments. The profile likelihood ratio λ as a function of
 520 annihilation cross-section $\langle\sigma v\rangle$ is computed by:

$$\lambda(\langle\sigma v\rangle | \mathcal{D}_{\text{dSphs}}) = \frac{\mathcal{L}(\langle\sigma v\rangle; \hat{\nu} | \mathcal{D}_{\text{dSphs}})}{\mathcal{L}(\widehat{\langle\sigma v\rangle}; \hat{\nu} | \mathcal{D}_{\text{dSphs}})} \quad (7.7)$$

522 for a considered annihilation channel and DM mass.

523 **TODO: Section pasted from paper. Rephrase cause plagiarism is a thing.** As mentioned pre-
 524 viously, each experiment computes the \mathcal{L}_{lk} from ?? differently. The remainder of this section
 525 highlights the differences in this calculation across the experiments. Four experiments, namely
 526 *Fermi*-LAT, H.E.S.S., HAWC and MAGIC, use a binned likelihood to compute the \mathcal{L}_{lk} . For these
 527 experiments, for each observation \mathcal{D}_{lk} of a given dSph l carried out using a given gamma-ray
 528 detector k , the binned likelihood function is:

$$\mathcal{L}_{lk}(\langle\sigma v\rangle; J_l, \nu_{lk} | \mathcal{D}_{lk}) = \prod_{i=1}^{N_E} \prod_{j=1}^{N_P} \left[\mathcal{P}(s_{lk,ij}(\langle\sigma v\rangle, J_l, \nu_{lk}) + b_{lk,ij}(\nu_{lk}) | N_{lk,ij}) \right] \times \mathcal{L}_{lk,\nu}(\nu_{lk} | \mathcal{D}_{\nu_{lk}}) \quad (7.8)$$

529 where N_E and N_P are the number of considered bins in reconstructed energy and arrival
 530 direction, respectively; \mathcal{P} represents a Poisson PDF for the number of gamma-ray candidate events
 531 $N_{lk,ij}$ observed in the i -th bin in energy and j -th bin in arrival direction, when the expected number
 532 is the sum of the expected mean number of signal events s_{ij} (produced by DM annihilation) and of
 533 background events b_{ij} ; $\mathcal{L}_{lk,\nu}$ is the likelihood term for the extra ν_{lk} nuisance parameters that vary
 534 from one instrument k to another. The expected counts for signal events s_{ij} for a given dSph l and
 535 detector k is given by:

$$s_{ij}(\langle\sigma v\rangle, J) = \int_{E'_{\min,i}}^{E'_{\max,i}} dE' \int_{P'_{\min,j}}^{P'_{\max,j}} d\Omega' \int_0^\infty dE \int_{\Delta\Omega_{tot}} d\Omega \int_0^{T_{\text{obs}}} dt \frac{d^2\Phi(\langle\sigma v\rangle, J)}{dEd\Omega} \text{IRF}(E', P' | E, P, t) \quad (7.9)$$

536 where E' and E are the reconstructed and true energies, P' and P the reconstructed and true
 537 arrival directions; $E'_{\min,i}$, $P'_{\min,j}$, $E'_{\max,i}$, and $P'_{\max,j}$ are their lower and upper limits of the i -th
 538 energy bin and the j -th arrival direction bin; T_{obs} is the (dead-time corrected) total observation

539 time; t is the time along the observations; $d^2\Phi/dEd\Omega$ is the DM flux in the source region (see
 540 ??); and $\text{IRF}(E', P' | E, P, t)$ is the IRF, which can be factorized as the product of the effective
 541 collection area of the detector $A_{\text{eff}}(E, P, t)$, the PDFs for the energy estimator $f_E(E' | E, t)$, and
 542 arrival direction $f_P(P' | E, P, t)$ estimators. Note that for Fermi-LAT, HAWC, MAGIC, and
 543 VERITAS the effect of the finite angular resolution is taken into account through the convolution of
 544 $d\Phi/dEd\Omega$ with f_P in ??, whereas in the cases of H.E.S.S. f_P is approximated by a delta function.
 545 This approximation has been made in order to maintain compatibility of the result with what
 546 has been previously published. The difference introduced by this approximation is $< 5\%$ for all
 547 considered dSphs. **TODO: End of paper section**

548 From ??, we can compute the test statistic (TS) with the ratio test:

$$\text{TS} = -2 \ln \left(\frac{\mathcal{L}}{\mathcal{L}^{\max}} \right). \quad (7.10)$$

549 \mathcal{L}^{\max} here is equivalent to $\mathcal{L}(N_i, B_i, S_i = 0)$ or no signal counts.

550 7.4 HAWC Results

551 13 of the 20 dSphs considered for the Glory Duck analysis are within HAWC's field of view.
 552 These dSph are analyzed for emission from DM annihilation according to the likelihood method
 553 described in ?. The 13 likelihood profiles are then combined to create a combined limit on the
 554 dark matter cross-section. This combination is done for the 7 annihilation channels used in the
 555 Glory Duck analysis. ? shows the combined limit for all annihilation channels with HAWC only
 556 observations. We also perform 300 studies of Poisson trials on the background. These trials are
 557 used to produce HAWC Brazil bands which were shared with the other collaborators for combined
 558 Brazil Bands. The results on fitting to HAWC's poisson trials of the DM hypothesis is shown in ??
 559 for seven of the DM annihilation channels.

560 No DM was found in HAWC observations. The limits are dominated by the dSph Segue1 and
 561 Coma Berenices. The remaining 11 dSphs do no contribute significantly to the limit. Even though
 562 some of the remaining dSphs have large J-factors, they are towards the edge of HAWC's field of
 563 view where this analysis is less sensitive.

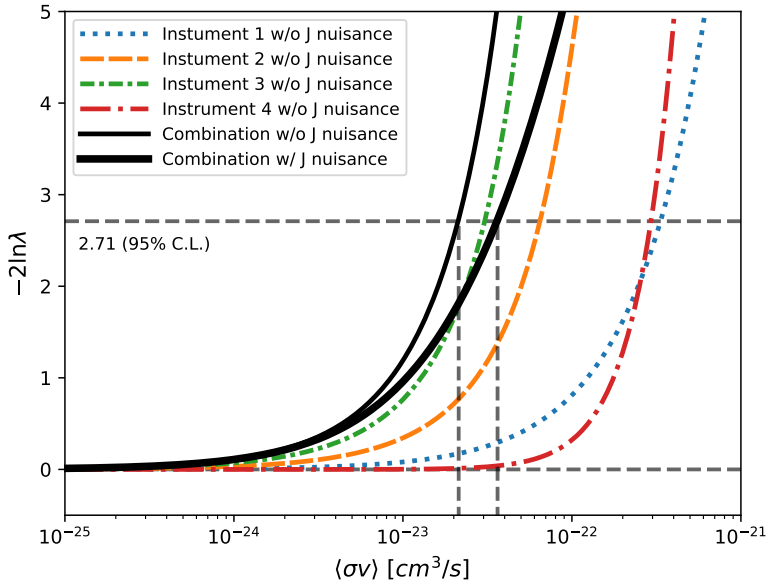


Figure 7.4 Illustration of the combination technique showing a comparison between $-2 \ln \lambda$ provided by four instruments (colored lines) from the observation of the same dSph without any J nuisance and their sum, *i.e.* the resulting combined likelihood (thin black line). According to the test statistics of ??, the intersection of the likelihood profiles with the line $-2 \ln \lambda = 2.71$ indicates the 95% C.L. upper limit on $\langle \sigma v \rangle$. The combined likelihood (thin black line) shows a smaller value of upper limit on $\langle \sigma v \rangle$ than those derived by individual instruments. We also show the uncertainties on the J -factor affects the combined likelihood and degrade the upper limit on $\langle \sigma v \rangle$ (thick black line). All likelihood profiles are normalized so that the global minimum $\widehat{\langle \sigma v \rangle}$ is 0. We note that each profile depends on the observational conditions in which a target object was observed. The sensitivity of a given instrument can be degraded and the upper limits less constraining if the observations are performed in non optimal conditions such as a high zenith angle or a short exposure time.

564 7.5 Glory Duck Combined Results

565 The crux of this analysis is that HAWC's results are combined with 4 other gamma-ray obser-
 566 vatories: Fermi-LAT, H.E.S.S., MAGIC, and VERITAS. The complete joint likelihood for the l -th
 567 dSph is the product of likelihood functions of the 5 experiments.

568 **TODO: place holder for results**

569 The *partial* joint likelihood function for gamma-ray observations of each dSph ($\mathcal{L}_{\text{dSph},l}$) is
 570 written as the product of the likelihood terms describing the $N_{\text{exp},l}$ observations performed with
 571 any of our observatories:

$$\mathcal{L}_{\text{dSph},l} ($$

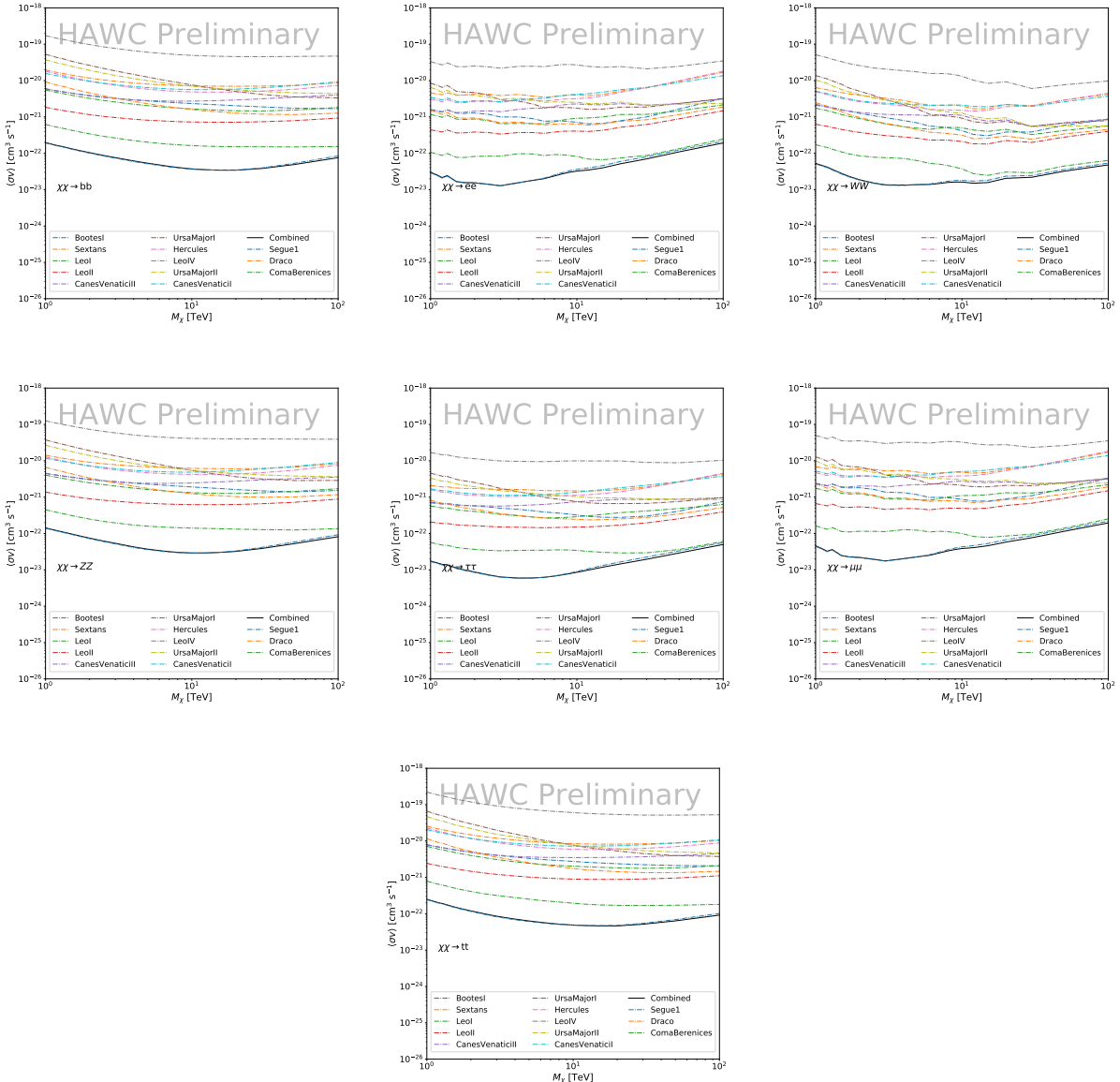


Figure 7.5 HAWC upper limits at 95% confidence level on $\langle\sigma v\rangle$ versus DM mass for seven annihilation channels, using the set of J -factors from Ref. [47]. The solid line represents the observed combined limit. Dashed lines represent limits from individual dSphs.

572 $\langle\sigma v\rangle; J_l, \nu_l \mid \mathcal{D}_l = \prod_{k=1}^{N_{\text{exp},l}} \mathcal{L}_{lk} (\langle\sigma v\rangle; J_l, \nu_{lk} \mid \mathcal{D}_{lk}, (7.11)$ where each \mathcal{L}_{lk} term refers to an
 573 observation of the l -th dSph with associated k -th instrument responses. $N_{\text{exp},l}$ varies from dSph to
 574 dSph and can be retrieved from ??.

575 Each collaboration separately analyses their data for \mathcal{D}_{lk} corresponding to dSph l and
 576 gamma-ray detector k , using as many common assumptions as possible in the analysis (see

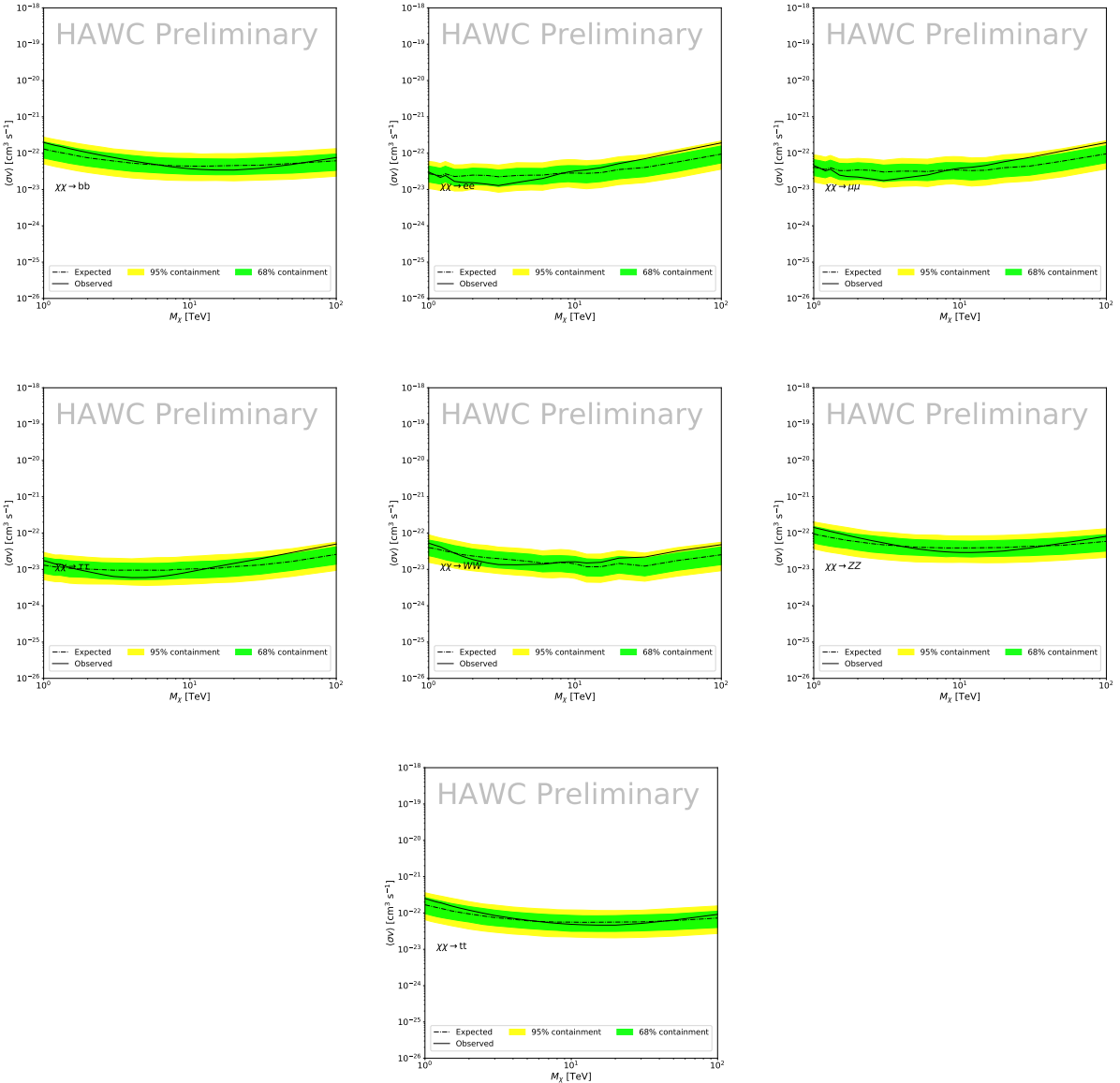


Figure 7.6 HAWC Brazil bands at 95% confidence level on $\langle\sigma v\rangle$ versus DM mass for seven annihilation channels with J -factors from \mathcal{GS} [47]. The solid line represents the combined limit from 13 dSphs. The dashed line is the expected limit. The green band is the 68% containment. The yellow band is the 95% containment.

the next paragraph and further down in this section for additional details). We compute the values for the likelihood functions \mathcal{L}_{lk} (see ??) for a fixed value of J_l and profile over the rest of the nuisance parameters ν_{lk} . Then, values of λ from ?? are computed as a function of $\langle\sigma v\rangle$, and shared using a common format. Results are recomputed for seven annihilation channels, W^+W^- , ZZ , $b\bar{b}$, $t\bar{t}$, e^+e^- , $\mu^+\mu^-$, and $\tau^+\tau^-$ over 62 m_χ values between 5 GeV and 100 TeV provided

582 in [Cirelli]. The $\langle\sigma v\rangle$ range is defined between 10^{-28} and $10^{-18} \text{ cm}^3 \cdot \text{s}^{-1}$, with 1001 logarithmically spaced values. The likelihood combination, i.e. ??, and profile over the J -factor to compute
 583 the profile likelihood ratio λ , ??, are carried out with two different public analysis software pack-
 584 ages, namely `gLike` [[javier_rico_2021_4601451](#)] and `LklCom` [[tjark_miener_2021_4597500](#)],
 585 that provide the same results [[2021arXiv211201818M](#)].

587 No significant DM emission was observed by any of the five telescopes. We present upper
 588 limits on $\langle\sigma v\rangle$ using the test statistics, ??.

$$\text{TS} = -2 \ln \lambda(\langle\sigma v\rangle), \quad (7.12)$$

589 No significant DM emission was observed by any of the five instruments. We present the upper
 590 limits on $\langle\sigma v\rangle$ assuming seven independent DM self annihilation channels, namely W^+W^- , Z^+Z^- ,
 591 $b\bar{b}$, $t\bar{t}$, e^+e^- , $\mu^+\mu^-$, and $\tau^+\tau^-$. The 68% and 95% containment bands are produced from 300
 592 Poisson realizations of the null hypothesis corresponding to each of the combined datasets. These
 593 300 realizations are combined identically to dSph observations. The containment bands and the
 594 median are extracted from the distribution of resulting limits on the null hypothesis. These 300
 595 realizations are obtained either by fast simulations of the OFF observations, for H.E.S.S., MAGIC,
 596 VERITAS, and HAWC, or taken from real observations of empty fields of view in the case of
 597 Fermi-LAT [48, 49, 50].

598 The obtained limits are shown in ?? for the $\mathcal{G}\mathcal{S}$ set of J -factors [47] and in ?? for the \mathcal{B} set of
 599 J -factors [46, 51]. The combined limits are presented with their 68% and 95% containment bands,
 600 and are expected to be close to the median limit when no signal is present. We observe agreement
 601 with the null hypothesis for all channels, within 2σ standard deviations, between the observed
 602 limits and the expectations given by the median limits. Limits obtained from each detector are also
 603 indicated in the figures, where limits for all dSphs observed by the specific instrument have been
 604 combined.

605 Below ~ 300 GeV, the *Fermi*-LAT dominates the DM limits for all annihilation channels. From
 606 ~ 300 GeV to ~ 2 TeV, *Fermi*-LAT continues to dominate for the hadronic and bosonic DM channels,

yet the IACTs (H.E.S.S., MAGIC, and VERITAS) and *Fermi*-LAT all contribute to the limit for leptonic DM channels. For DM masses between ~ 2 TeV to ~ 10 TeV, the IACTs dominate leptonic DM annihilation channels, whereas both the *Fermi*-LAT and the IACTs dominate bosonic and hadronic DM annihilation channels. From ~ 10 TeV to ~ 100 TeV, both the IACTs and HAWC contribute significantly to the leptonic DM limit. For hadronic and bosonic DM, the IACTs and *Fermi*-LAT both contribute strongly.

We notice that the limits computed using the \mathcal{B} set of J -factor are always better compared to the ones calculated with the \mathcal{GS} set. For the W^+W^- , Z^+Z^- , $b\bar{b}$, and $t\bar{t}$ channels, the ratio between the limits computed with the two sets of J -factor is varying between a factor of ~ 3 and ~ 5 depending on the energy, with the largest ratio around 10 TeV. For the channels e^+e^- , $\mu^+\mu^-$, and $\tau^+\tau^-$, the ratio lies between ~ 2 to ~ 6 , being maximum around 1 TeV. Examining ?? and ?? in ??, these differences are explained by the fact that the \mathcal{B} set provides higher J -factors for the majority of the studied dSphs, with the notable exception of Segue I. The variation on the ratio of the limits for the two sets is due to different dSph dominating the limits depending on the energy. This pushes the range of thermal cross-section which can be excluded to higher mass. This comparison demonstrates the magnitude of systematic uncertainties associated with the choice of the J -factor

This comparison demonstrates the magnitude of systematic uncertainties associated with the choice of the J -factor calculation. The \mathcal{GS} and \mathcal{B} sets present a difference in the limits for all channels of about This difference is explained, see ?? and ?? in Appendix, by the fact that the \mathcal{B} set provides higher J factors for all dSph except for Segue I. This pushes the range of thermal cross-section which can be excluded to higher mass.

7.6 HAWC Systematics

7.6.1 Inverse Compton Scattering

The DM-DM annihilation channels produce many high energy electrons regardless of the primary annihilation channel. These high energy electrons can produce high energy gamma-rays through Inverse Compton Scattering (ICS). If this effect is strong, it would change the morphology of the source and increase the total expected gamma-ray counts from any source. The PPPC [43]

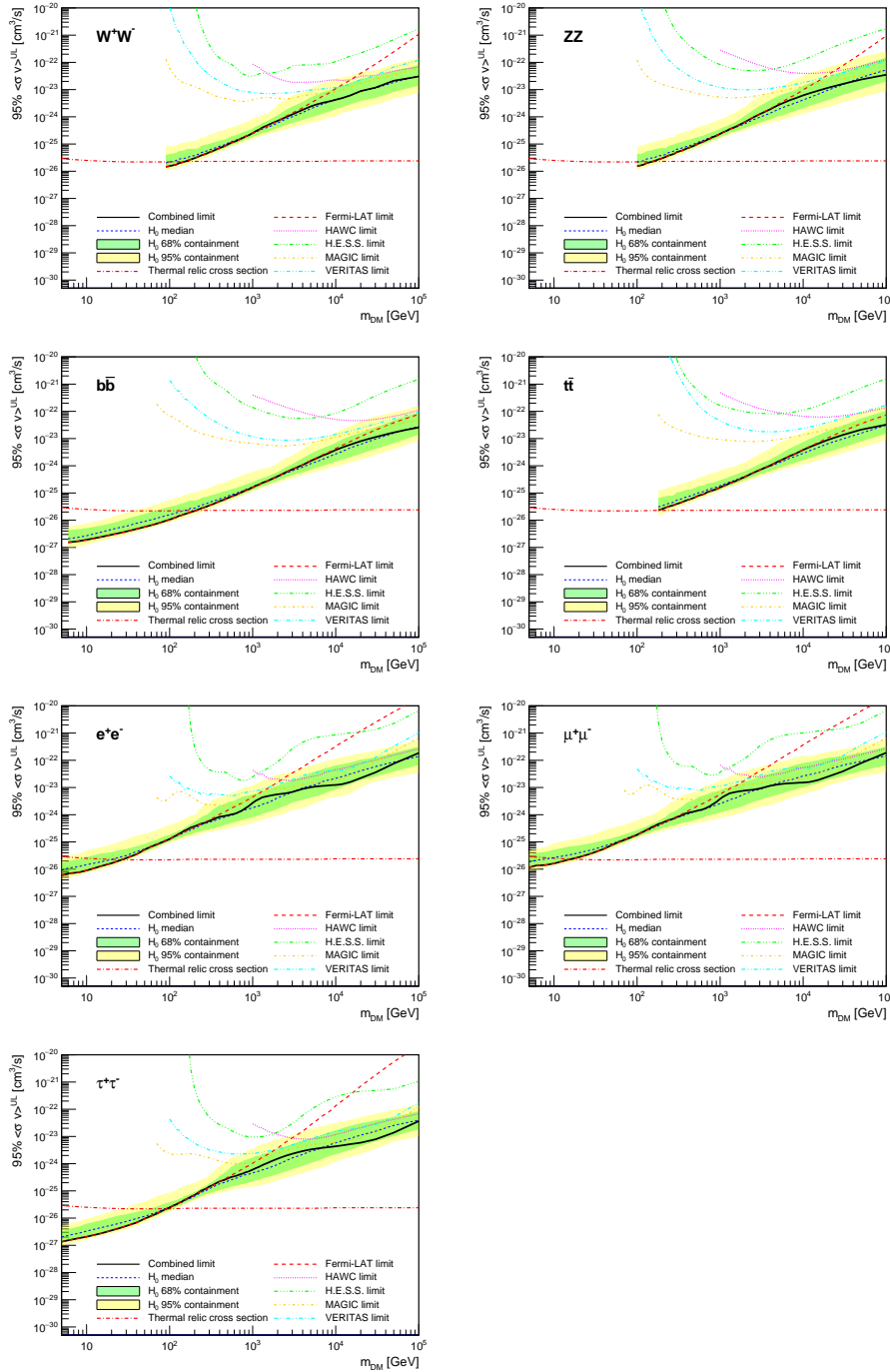


Figure 7.7 Upper limits at 95% confidence level on $\langle \sigma v \rangle$ in function of the DM mass for eight annihilation channels, using the set of J factors from Ref. [47] (\mathcal{GS} set in ??). The black solid line represents the observed combined limit, the black dashed line is the median of the null hypothesis corresponding to the expected limit, while the green and yellow bands show the 68% and 95% containment bands. Combined upper limits for each individual detector are also indicated as solid, colored lines. The value of the thermal relic cross-section in function of the DM mass is given as the red dotted-dashed line [52].

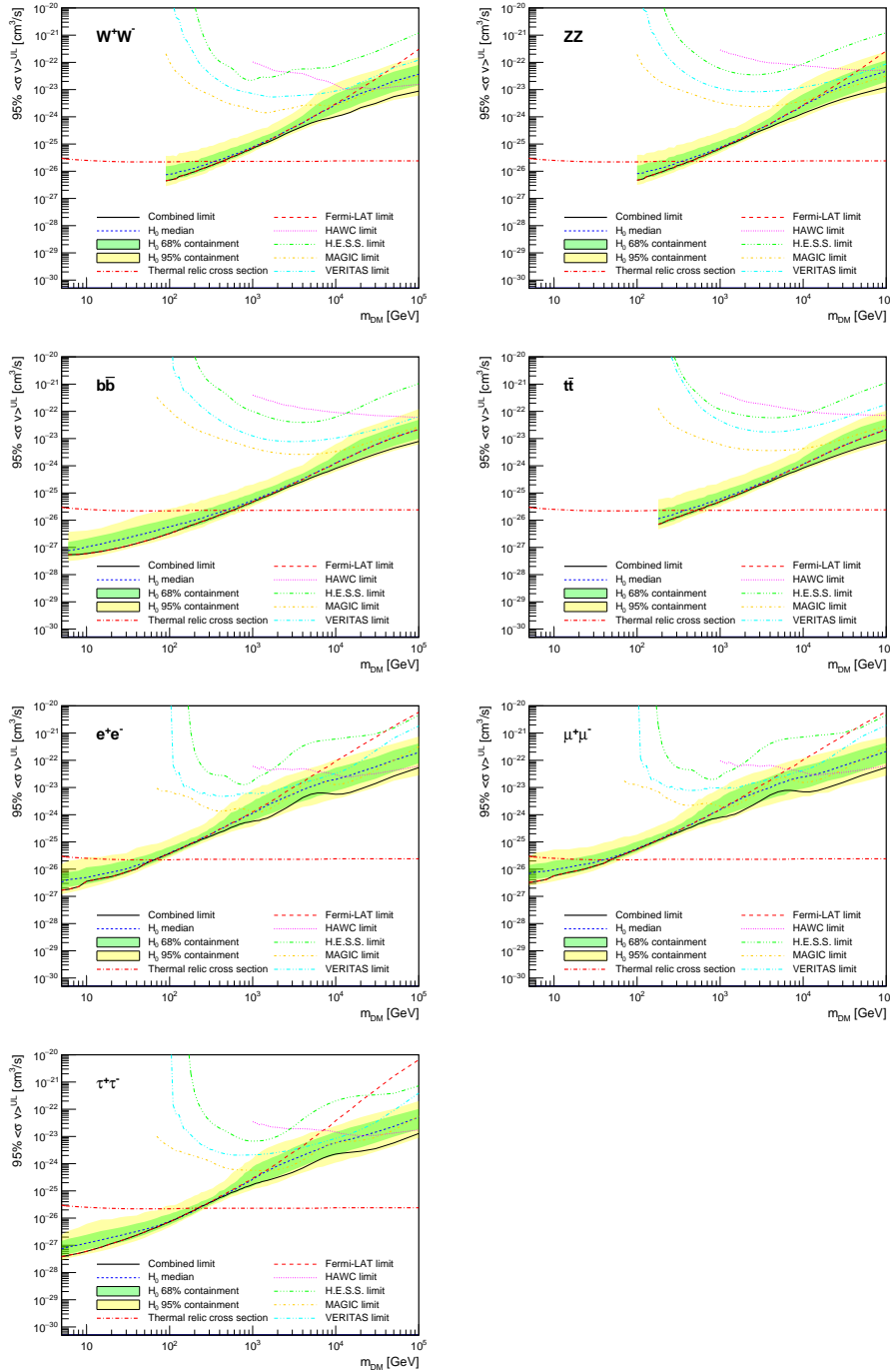


Figure 7.8 Same as ??, using the set of J factors from Ref. [46, 51] (\mathcal{B} set in ??).

provides tools in Mathematica for calculating the impact of ICS for an arbitrary location in the sky for a specified annihilation channel. We calculated the change in gamma-ray counts for DM annihilation to primary $e\bar{e}$ for RA and Dec corresponding to Segue1 and Coma Berenices. These dSphs were chosen because they are the strongest contributors to the limit. $e\bar{e}$ was selected because

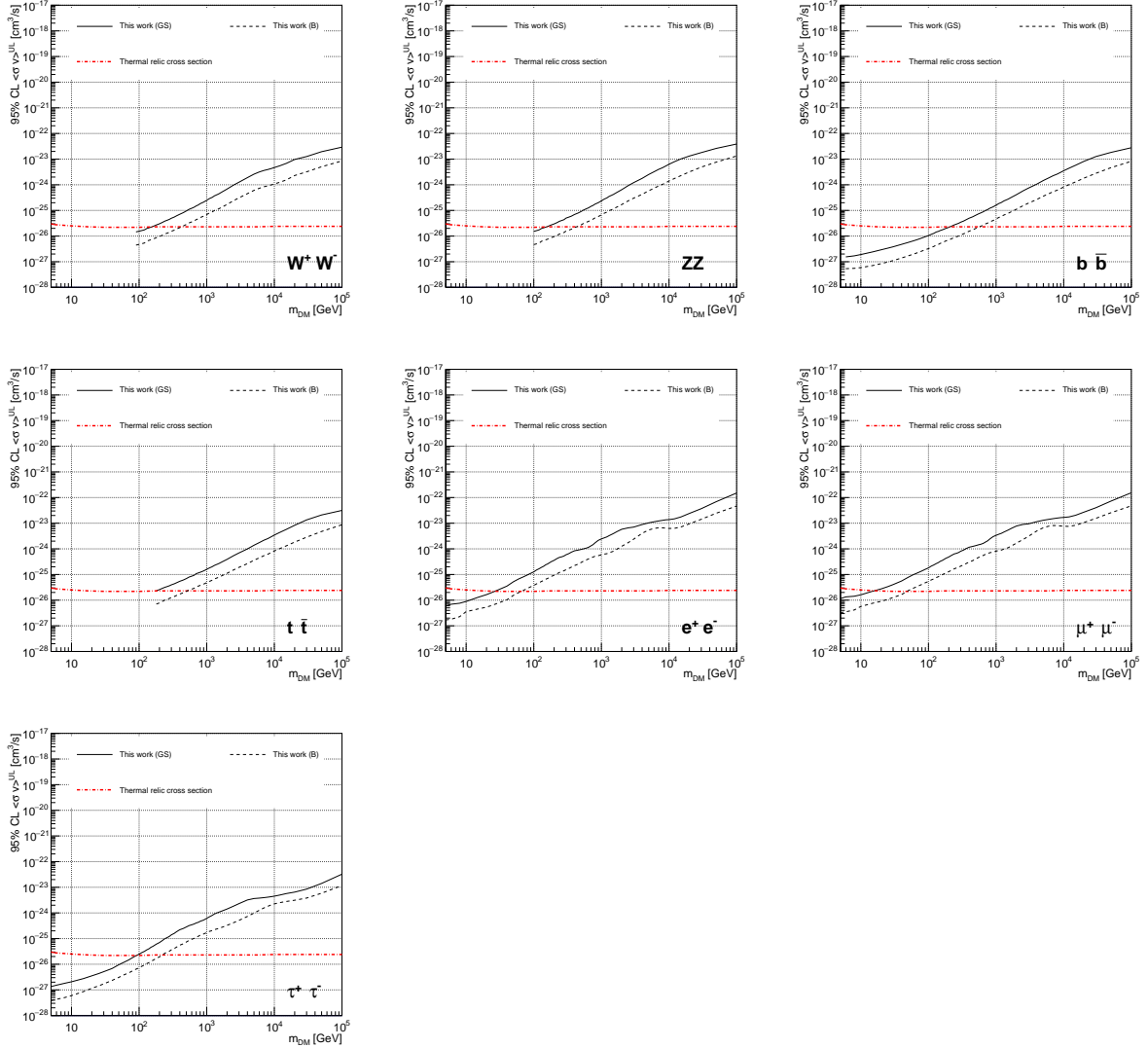


Figure 7.9 Comparisons of the combined limits at 95% confidence level for each of the eight annihilation channels when using the J factors from Ref. [47] (\mathcal{GS} set in ??), plain lines, and the J factor from Ref. [46, 51] (\mathcal{B} set in ??), dashed lines. The cross-section given by the thermal relic is also indicated [52].

it would have the largest number of high energy electrons. The effect was found to be on the order of 10^{-7} on the gamma-ray spectrum. As a result, this systematic is not considered in our analysis.

7.6.2 Point Source Versus Extended Source Limits

The previous DM search toward dSph approximated the dSphs as point sources [45]. In this analysis, the dSphs are implemented as extended with J-factor distributions following those produced by [47]. The resolution of the cited map is much finer than HAWC's angular resolution.

644 The vast majority of the J-factor distribution is represented on the central HAWC pixel of the dSph
 645 spatial map. However, the neighboring 8 pixels are not negligible and contribute to our limit.

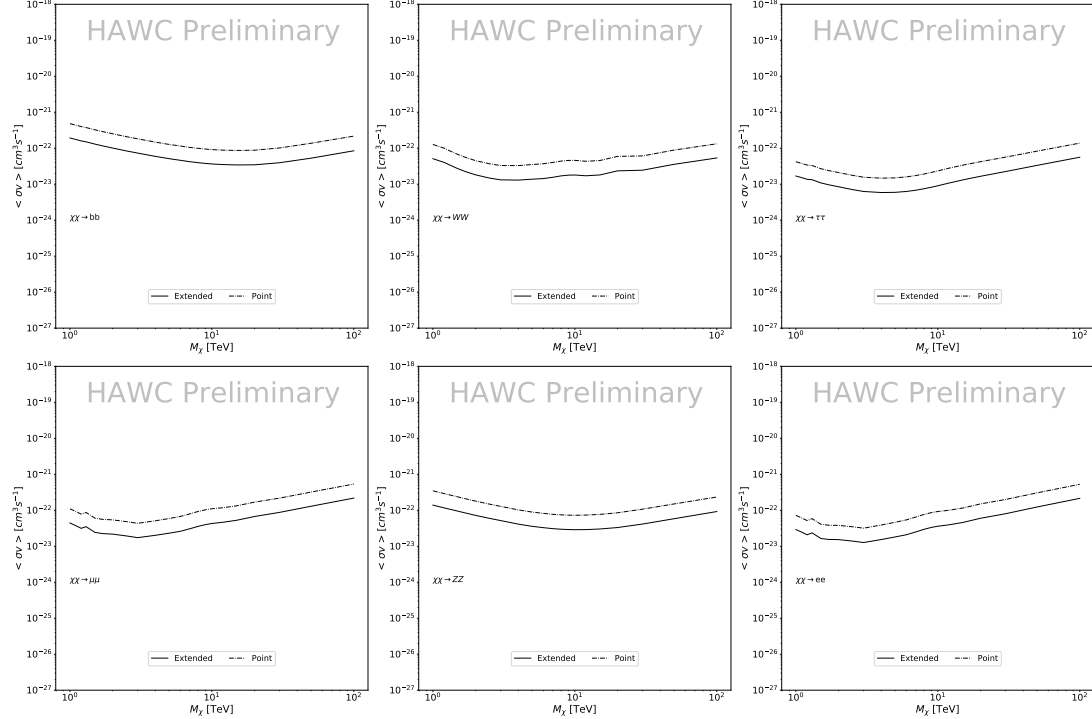


Figure 7.10 Comparisons of the combined limits at 95% confidence level for a point source analysis and extended source using [47] $\mathcal{G}\mathcal{S}$ J-factor distributions and PPPC [43] annihilation spectra. Shown are the limits for Segue1 which will have the most significant impact on the combined limit. 6 of the 7 DM annihilation channels are shown. Solid lines are extended source studies. Dashed lines are point source studies. Overall, the extended source analysis improves the limit by a factor of 2.

646 ?? shows a substantial improvement to the limit for Segue1. ?? however showed identical
 647 limits. These disparities are best explained by the relative difference in their J-Factors. Both dSphs
 648 pass almost overhead the HAWC detector, however Segue1 has the larger J-Factor between the two.
 649 Adjacent pixels to the central pixel will therefore contribute to the limits. This is the case for other
 650 dSph that are closer to overhead the HAWC detector.

651 Comparison plots for all sources and the combined limit can be found in the sandbox for the
 652 Glory Duck project.

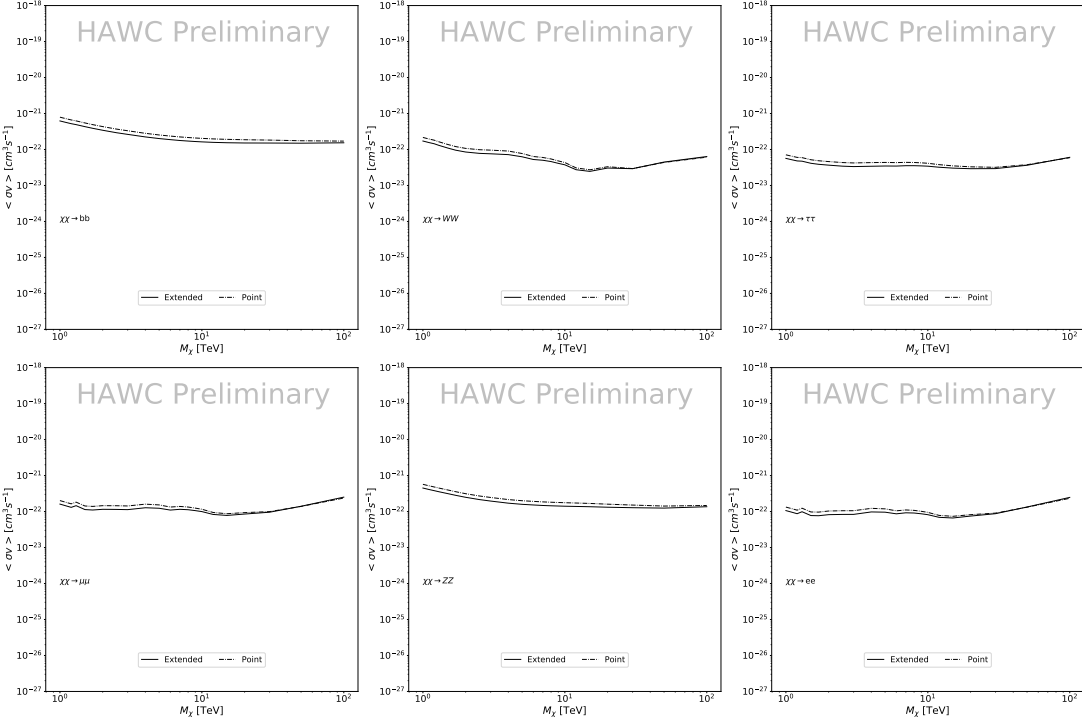


Figure 7.11 Same as ?? on Coma Berenices. This dSph also contributes significantly to the limit. The limits are identical in this case.

653 7.6.3 Impact of Pointing Systematic

654 During the analysis it was discovered that reconstruction of gamma-rays. Slides describing this
 655 systematic can be found [here](#). Shown on the presentation is dependence on the pointing systematic
 656 on declination. New spatial profiles were generated for every dSph and limits were computed for
 657 the adjusted declination.

658 ?? demonstrates the impact of this systematic for all DM annihilation channels studied by
 659 HAWC. The impact is a tiny improvement, yet mostly identical, to the combined limits.

660 7.7 J-factor distributions

661 7.7.1 Numerical integration of \mathcal{GS} maps

662 It was discovered well after the HAWC analysis was completed that the published tables from
 663 \mathcal{GS} [44] quoted median J -factors were computed in a non-trivial manner. The assumption myself
 664 and collaborators had was that the published tables represented the J -factor as a function of θ for
 665 the best global fit model on a per source basis. However, this is not the case. Instead, what is

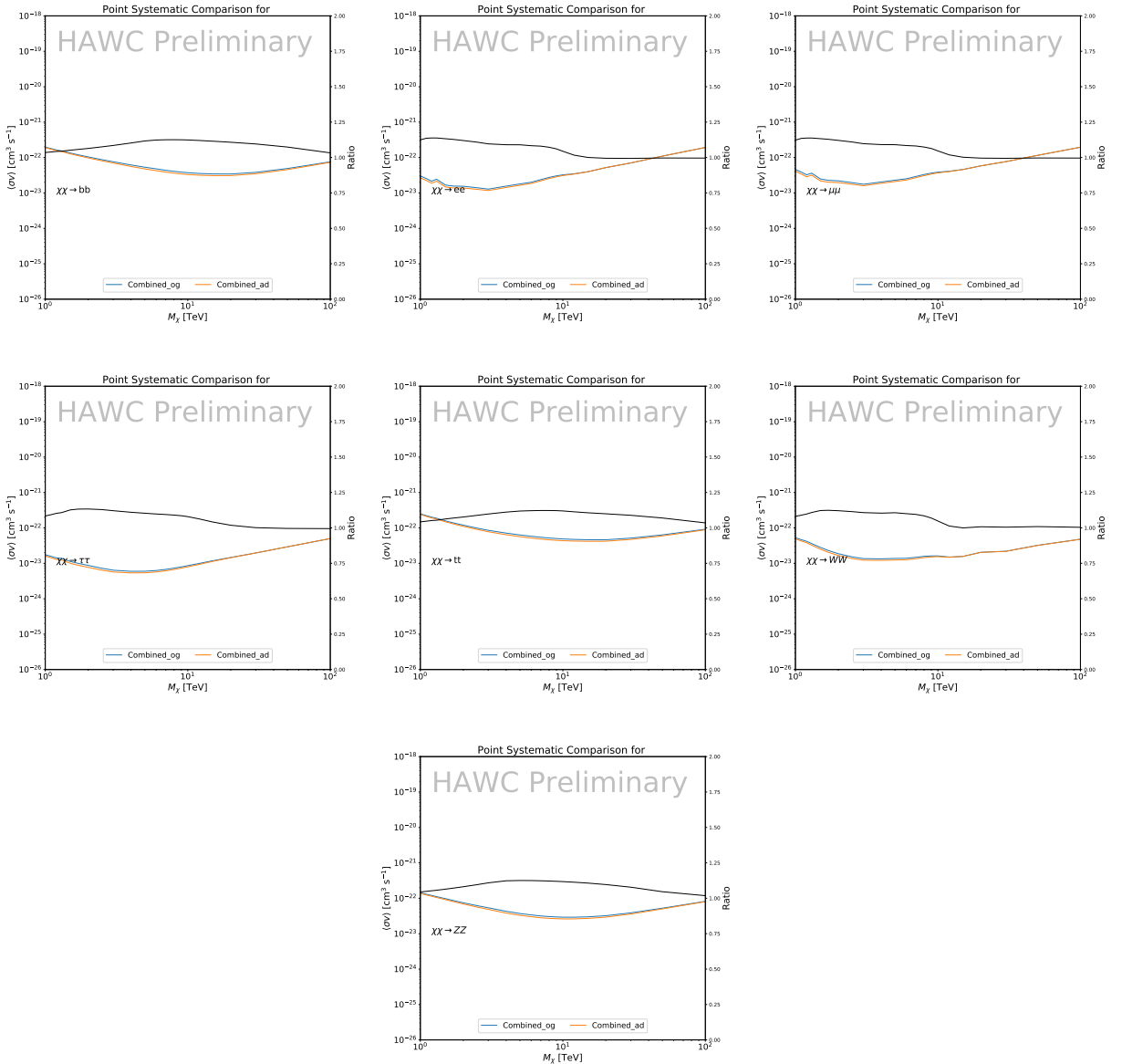


Figure 7.12 Comparison of combined limits when correcting for HAWC's pointing systematic. All DM annihilation channels are shown. The solid black line is the ratio between published limit to the declination corrected limit. The blue solid line or "Combined_og" represented the limits computed for Glory Duck. The solid orange line or "Combined_ad" represented the limits computed after correcting for the pointing systematic.

published are the best fit model for each dwarf that only considers stars up to the angular separation θ . Therefore, the model is changing for each value of θ for each dwarf. Yet, the introduced features from unique models at each θ are much smaller than the angular resolution of HAWC. It is not expected for these effects to impact the limits and TS greatly as a result.

670 Median J -factor model profiles were provided by the authors. New maps were generated and
671 analyzed for Segue1 and Coma Berenices. ?? shows the differential between maps generated with
672 the method from ?? and from the authors of [44]. These maps were reanalyzed for all SM DM
673 annihilation channels. Upper limits for these channels are shown in ??

674 From ??, we can see that the impact of these model difference was no substantial. The observed
675 impact was a fractional effect which is much smaller than the impact from selecting another DM
676 spatial distribution model as was shown in ??.

677 **7.7.2 \mathcal{GS} versus \mathcal{B} spatial models**

678 We show in this appendix a comparison between the J -factors computed by Geringer-Sameth
679 *et al.* [47] (the \mathcal{GS} set) and the ones computed by Bonnivard *et al.* [46, 51] (the \mathcal{B} set). The
680 \mathcal{GS} J -factors are computed through a Jeans analysis of the kinematic stellar data of the selected
681 dSphs, assuming a dynamic equilibrium and a spherical symmetry for the dSphs. They adopted
682 the generalized DM density distribution, known as Zhao-Hernquist, introduced by [53], carrying
683 three additional index parameters to describe the inner and outer slopes, and the break of the
684 density profile. Such a profile parametrization allows the reduction of the theoretical bias from
685 the choice of a specific radial dependency on the kinematic data. In other words, the increase of
686 free parameters with the use of the Zhao-Hernquist profile allows a better description of the mass
687 density distribution of dark matter.

688 In addition, a constant velocity anisotropy profile and a Plummer light profile [54] for the stellar
689 distribution were assumed. The velocity anisotropy profile depends on the radial and tangential
690 velocity dispersions. However, its determination remains challenging since only the line-of-sight
691 velocity dispersion can be derived from velocity measurements. Therefore, the parametrization of
692 the anisotropy profile is obtained from simulated halos (see [55] for more details). They provide the
693 values of the J -factors of regions extending to various angular radius up to the outermost member
694 star.

695 The \mathcal{B} J -factors were computed through a Jeans analysis taking into account the systematic
696 uncertainties induced by the DM profile parametrization, the radial velocity anisotropy profile, and

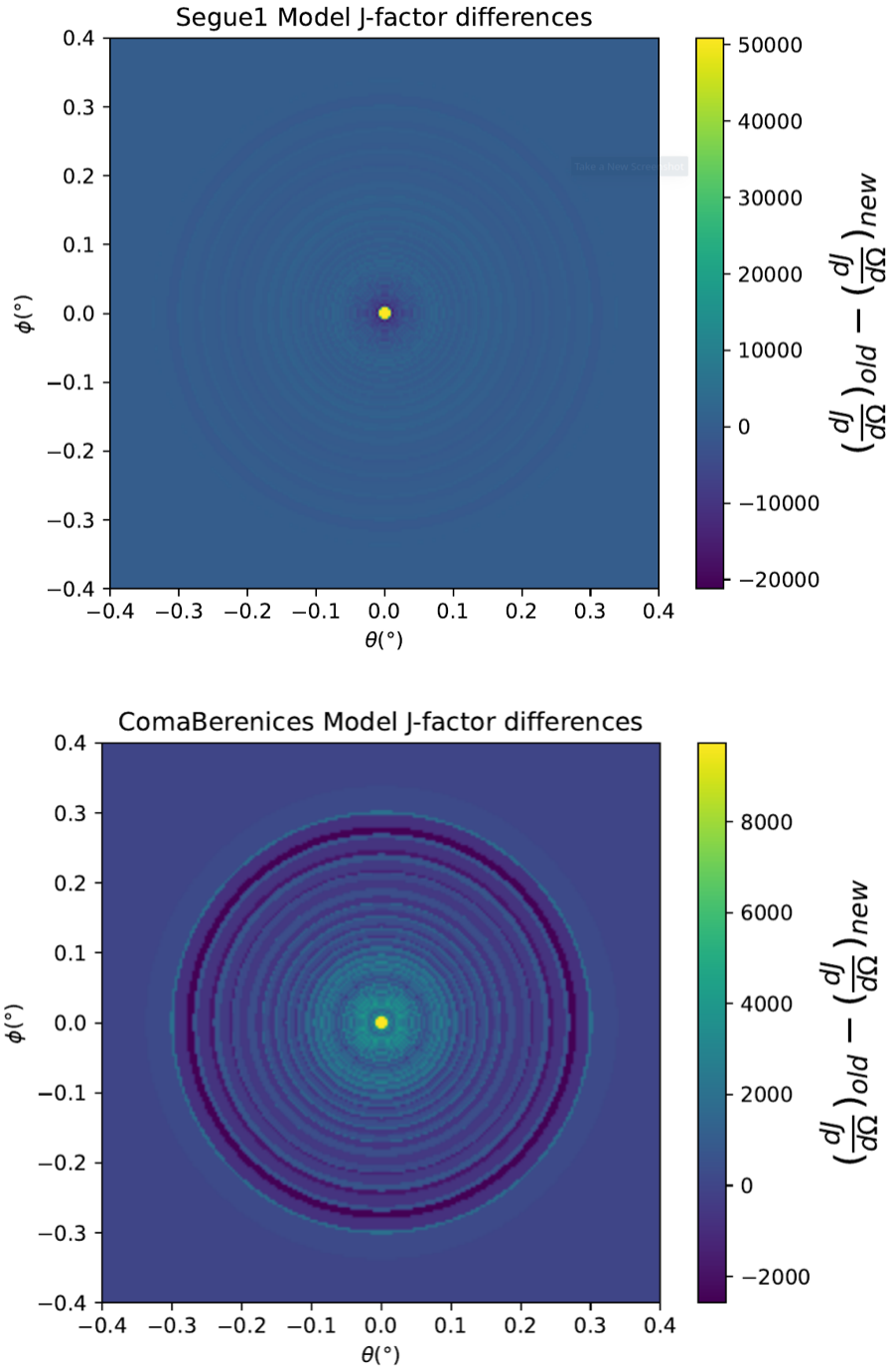


Figure 7.13 Differential map of dJ/Ω from model built in ?? and profiles provided directly from authors. (Top) Differential from Segue1. (bottom) Differential from Coma Berenices. Note that their scales are not the same. Segue1 shows the deepest discrepancies which is congruent with its large uncertainties. Both models show anuli where unique models become apparent.

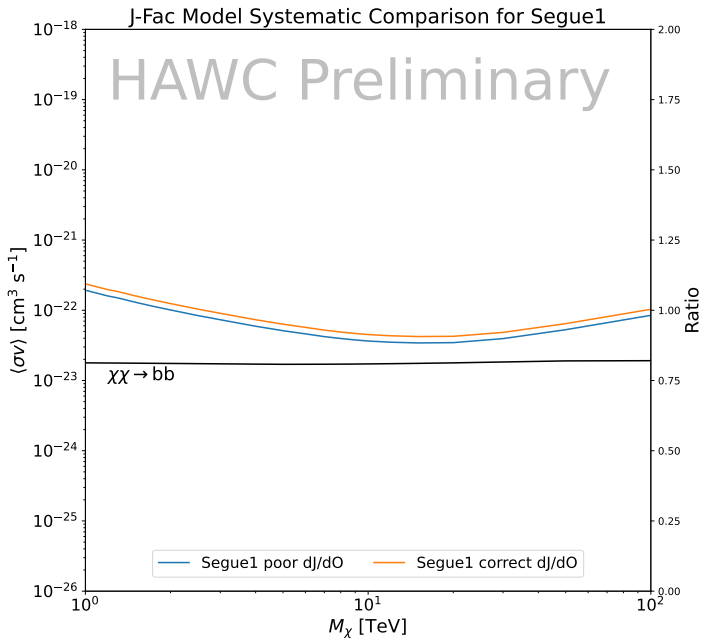
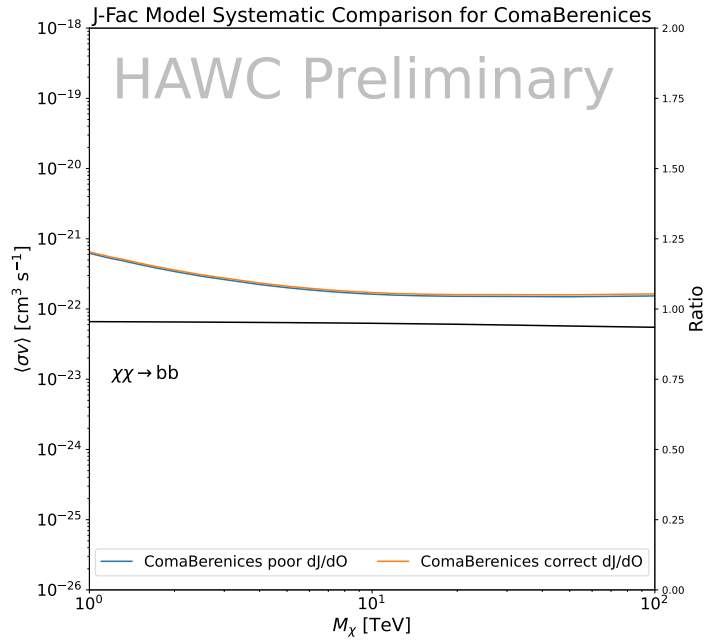


Figure 7.14 HAWC limits for Coma Berenices (top) and Segue1 (bottom) for two different map sets. Blue lines are limits calculated on maps with poor model representation. Orange lines are limits calculated on spatial profiles provided by the authors of [44]. Black line is the ratio of the poor spatial model limits to the corrected spatial models. The left y-axis measures $\langle \sigma v \rangle$ for the blue and orange lines. The right y-axis measures the ratio and is unitless.

697 the triaxiality of the halo of the dwarf galaxies. They performed a more complete study of the dSph
698 kinematics and dynamics than \mathcal{GS} for the determination of the J -factor. Conservative values of the
699 J -factors were obtained using an Einasto DM density profile [56], a realistic anisotropy profile
700 known as the Baes & Van Hese profile [57] which takes into account that the inner regions can be
701 significantly non-isotropic, and a Zhao-Hernquist light profile [53].

702 For both sets, J -factor values are provided for all dSphs as a function of the radius of the
703 integration region [47, 46, 51]. ?? shows the heliocentric distance and Galactic coordinates of the
704 twenty dSphs, together with the two sets of J -factor values integrated up to the outermost observed
705 star for \mathcal{GS} and the tidal radius for \mathcal{B} . Both J -factor sets were derived through a Jeans analysis
706 based on the same kinematic data, except for Draco where the measurements of [58] have been
707 adopted in the computation of the \mathcal{B} value. The computations for producing the \mathcal{GS} and \mathcal{B} samples
708 differ in the choice of the DM density, velocity anisotropy, and light profiles, for which the set \mathcal{B}
709 takes into account some sources of systematic uncertainties.

710 ?? and ?? show the comparisons for the J -factor versus the angular radius for each of the
711 20 dSphs used in this study. The uncertainties provided by the authors are also indicated in the
712 figures. For the \mathcal{GS} set, the computation stops at the angular radius corresponding to the outermost
713 observed star, while for the \mathcal{B} set, the computation stops at the angular radius corresponding to the
714 tidal radius.

715 7.8 Discussion and Conclusions

716 In this multi-instrument analysis, we have used observations of 20 dSphs from the gamma-ray
717 telescopes Fermi-LAT, H.E.S.S., MAGIC, VERITAS, and HAWC to perform a collective DM
718 search annihilation signals. The data were combined across sources and detectors to significantly
719 increase the sensitivity of the search. We have observed no significant deviation from the null, no
720 DM hypothesis, and so present our results in terms of upper limits on the annihilation cross section
721 for seven potential DM annihilation channels.

722 Fermi-LAT brings the most stringent constraints for continuum channels below approximately
723 1 TeV. the remaining detectors dominate at higher energies. Overall, for multi-TeV DM mass,

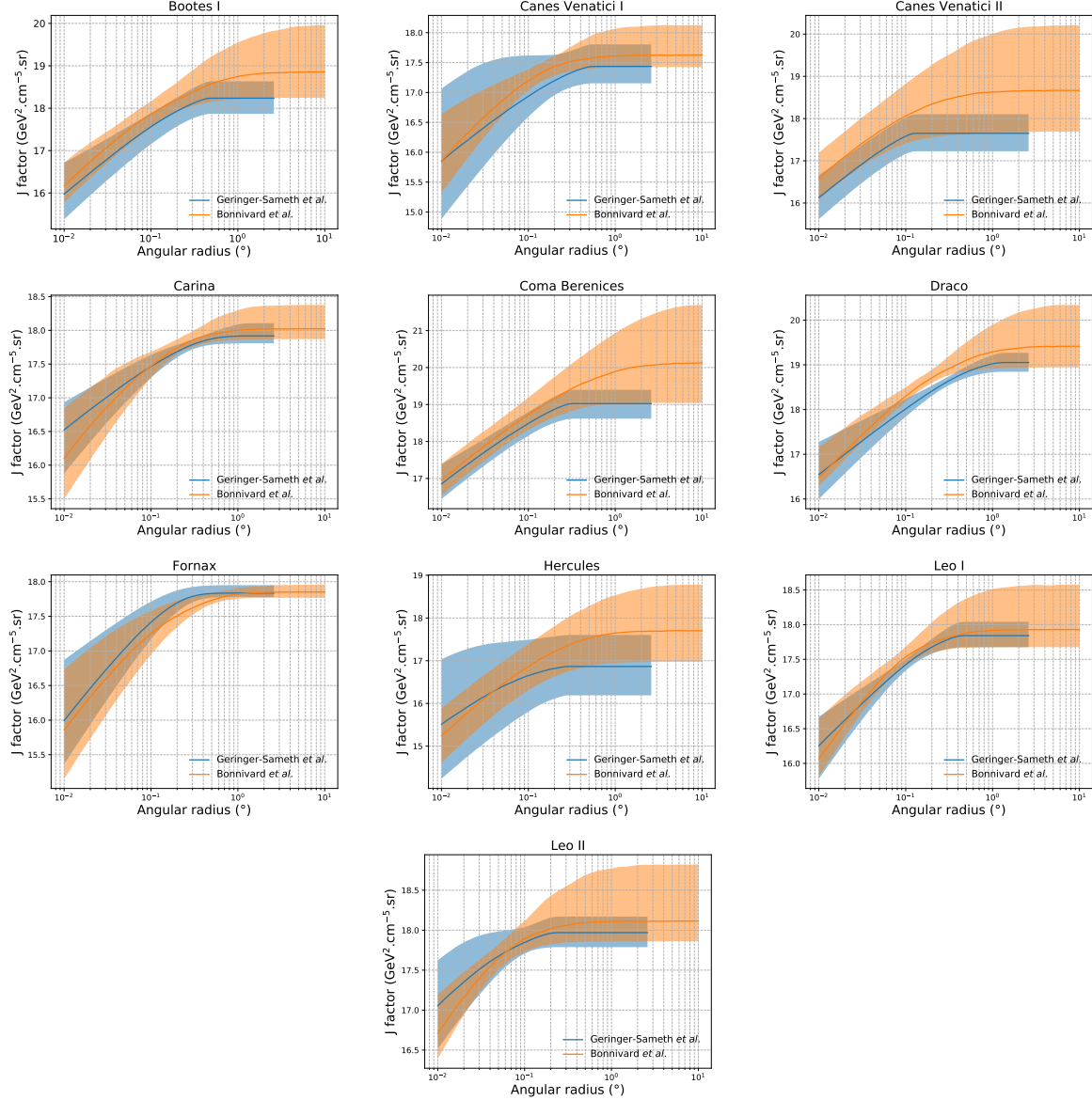


Figure 7.15 Comparisons between the J -factors versus the angular radius for the computation of J factors from Ref. [47] (\mathcal{GS} set in ??) in blue and for the computation from Ref. [46, 51] (\mathcal{B} set in ??) in orange. The solid lines represent the central value of the J -factors while the shaded regions correspond to the 1σ standard deviation.

the combined DM constraints from all five telescopes are 2-3 times stronger than any individual telescope for multi-TeV DM.

Derived from observations of many dSphs, our results produce robust limits given the DM content of the dSphs is relatively well constrained. The obtained limits span the largest mass range of any WIMP DM search. Our combined analysis improves the sensitivity over previously

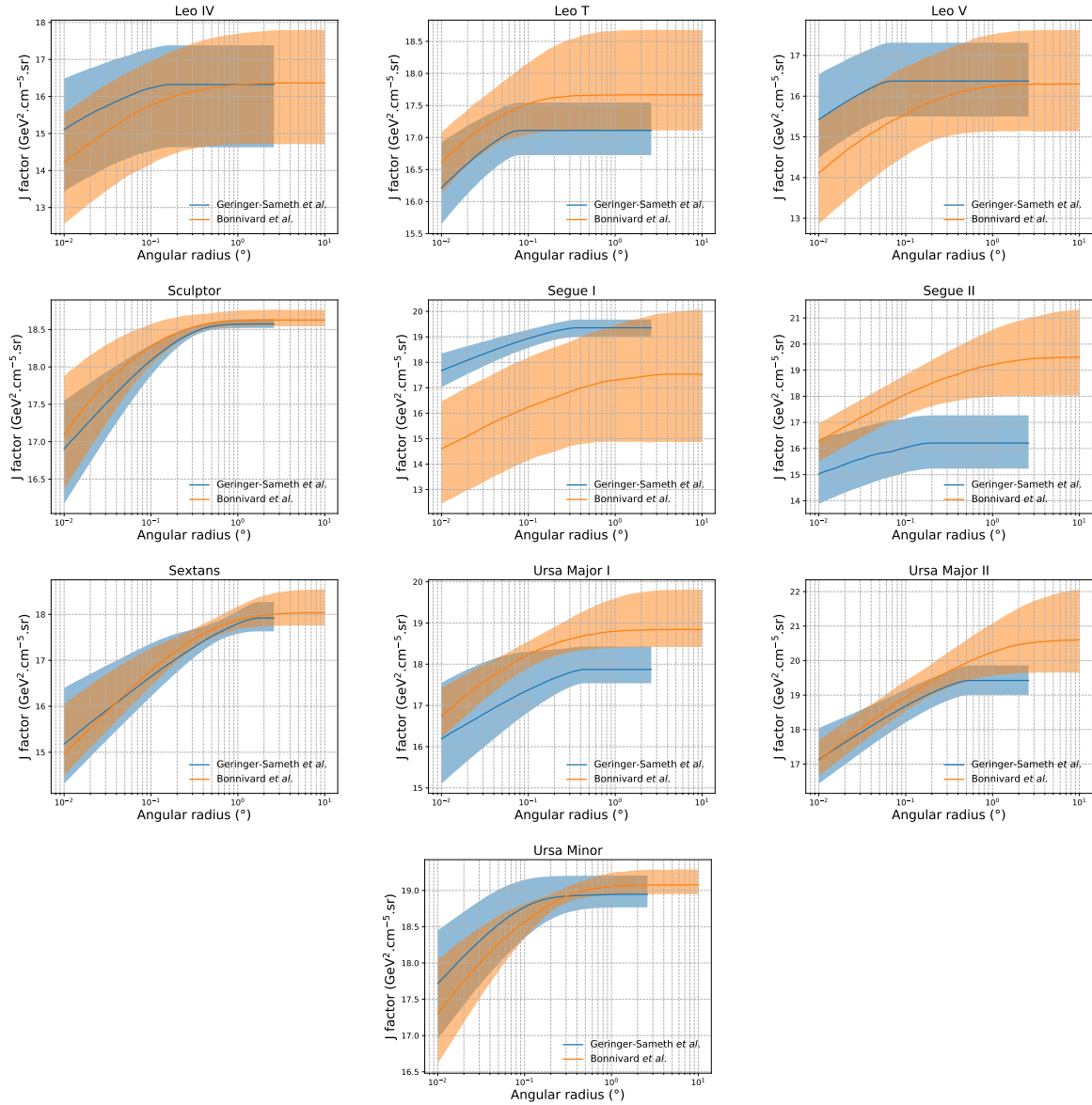


Figure 7.16 Comparisons between the J -factors versus the angular radius for the computation of J factors from Ref. [47] (\mathcal{GS} set in ??) in blue and for the computation from Ref. [46, 51] (\mathcal{B} set in ??) in orange. The solid lines represent the central value of the J -factors while the shaded regions correspond to the 1σ standard deviation.

729 published results from each detectors which produces the most stringent limits on DM annihilation
 730 from dSphs. These results are based on deep exposures of the most promising known dSphs with
 731 the currently most sensitive gamma-ray instruments. Therefore, our results constitute a legacy of
 732 a generation of gamma-ray instruments on WIMP DM searches towards dSphs. Our results will
 733 remain the reference in the field until a new generation of more sensitive gamma-ray instruments

734 begin operations, or until new dSphs with higher J -factors are discovered.

735 This analysis serves as a proof of concept for future multi-instrument and multi-messenger
736 combination analyses. With this collaborative effort, we have managed to sample over four orders
737 in magnitude in gamma-ray energies with distinct observational techniques. Determining the nature
738 of DM continues to be an elusive and difficult problem. Larger datasets with diverse measurement
739 techniques could be essential to tackling the DM problem. A future collaboration using similar
740 techniques as the ones described in this paper could grow even beyond gamma rays. The models we
741 used for this study include annihilation channels with neutrinos in the final state. Advanced studies
742 could aim to merge our results with those from neutrino observatories with large data sets. Efforts
743 are already underway to add data from the IceCube, ANTARES, and KM3NeT observatories to
744 these gamma-ray results.

745 From this work, a selection of the best candidates for observations, according to the latest
746 knowledge on stellar dynamics and modelling techniques for the derivation of the J -factors on the
747 potential dSphs targets, is highly desirable at the time that new experiments are starting their dark
748 matter programmes using dSphs. Given the systematic uncertainty inherent to the derivation of
749 the J -factors, an informed observational strategy would be to select both objects with the highest
750 J -factors that could lead to DM signal detection, and objects with robust J -factor predictions, i.e.
751 with kinematic measurements on many bright stars, which would strengthen the DM interpretation
752 reliability of the observation outcome.

753 This analysis combines data from multiple telescopes to produce strong constraints on astro-
754 physical objects. From this perspective, these methods can be applied beyond just DM searches.
755 Almost every astrophysical study can benefit from multi-telescope, multi-wavelength gamma-ray
756 studies. We have enabled these telescopes to study the cosmos with greater precision and detail.
757 Many astrophysical searches can benefit from multi-instrument gamma-ray studies, for which our
758 analysis lays the foundation.

CHAPTER 8**NU DUCK**

CHAPTER 9**MULTITHREADING HAWC ANALYSES FOR DARK MATTER SEARCHES**

BIBLIOGRAPHY

- 762 [1] Anne M. Green. “Dark matter in astrophysics/cosmology”. In: *SciPost Phys. Lect.*
 763 *Notes* (2022), p. 37. doi: [10.21468/SciPostPhysLectNotes.37](https://doi.org/10.21468/SciPostPhysLectNotes.37). URL: <https://scipost.org/10.21468/SciPostPhysLectNotes.37>.
- 765 [2] Bing-Lin Young. “A survey of dark matter and related topics in cosmology”. In: *Frontiers*
 766 *of Physics* 12 (Oct. 2016). doi: <https://doi.org/10.1007/s11467-016-0583-4>.
 767 URL: <https://doi.org/10.1007/s11467-016-0583-4>.
- 768 [3] Gianfranco Bertone, Dan Hooper, and Joseph Silk. “Particle dark matter: evidence,
 769 candidates and constraints”. In: *Physics Reports* 405.5 (2005), pp. 279–390. ISSN:
 770 0370-1573. doi: <https://doi.org/10.1016/j.physrep.2004.08.031>. URL:
 771 <https://www.sciencedirect.com/science/article/pii/S0370157304003515>.
- 772 [4] Gianfranco Bertone and Dan Hooper. “History of dark matter”. In: *Rev. Mod. Phys.*
 773 90 (4 Aug. 2018), p. 045002. doi: [10.1103/RevModPhys.90.045002](https://doi.org/10.1103/RevModPhys.90.045002). URL: <https://link.aps.org/doi/10.1103/RevModPhys.90.045002>.
- 775 [5] Fritz Zwicky. “The Redshift of Extragalactic Nebulae”. In: *Helvetica Physica Acta* 6.
 776 (1933), pp. 110–127. doi: [10.5169/seals-110267](https://doi.org/10.5169/seals-110267).
- 777 [6] Vera C. Rubin and Jr. Ford W. Kent. “Rotation of the Andromeda Nebula from a
 778 Spectroscopic Survey of Emission Regions”. In: *ApJ* 159 (Feb. 1970), p. 379. doi:
 779 [10.1086/150317](https://doi.org/10.1086/150317).
- 780 [7] K. G. Begeman, A. H. Broeils, and R. H. Sanders. “Extended rotation curves of spiral galaxies: dark haloes and modified dynamics”. In: *Monthly Notices of the Royal Astronomical Society* 249.3 (Apr. 1991), pp. 523–537. ISSN: 0035-8711. doi: [10.1093/mnras/249.3.523](https://doi.org/10.1093/mnras/249.3.523). eprint: <https://academic.oup.com/mnras/article-pdf/249/3/523/18160929/mnras249-0523.pdf>. URL: <https://doi.org/10.1093/mnras/249.3.523>.
- 785 [8] *Different types of gravitational lenses*. website. Feb. 2004. URL: <https://esahubble.org/images/heic0404b/>.
- 787 [9] Douglas Clowe et al. “A Direct Empirical Proof of the Existence of Dark Matter”. In: *apjl*
 788 648.2 (Sept. 2006), pp. L109–L113. doi: [10.1086/508162](https://doi.org/10.1086/508162). arXiv: [astro-ph/0608407](https://arxiv.org/abs/astro-ph/0608407)
 789 [[astro-ph](#)].
- 790 [10] Planck Collaboration and N. et. al. Aghanim. “Planck 2018 results I. Overview and the
 791 cosmological legacy of Planck”. In: *A&A* 641 (2020). doi: [10.1051/0004-6361/201833880](https://doi.org/10.1051/0004-6361/201833880). URL: <https://doi.org/10.1051/0004-6361/201833880>.
- 793 [11] Wayne Hu. *Matter Density Animation*. web. 2024. URL: <http://background.uchicago.edu/~whu/animbut/anim2.html>.

- 795 [12] Wenlong Yuan et al. “A First Look at Cepheids in a Type Ia Supernova Host with JWST”. in:
796 *The Astrophysical Journal Letters* 940.1 (Nov. 2022). doi: [10.3847/2041-8213/ac9b27](https://doi.org/10.3847/2041-8213/ac9b27).
797 URL: <https://dx.doi.org/10.3847/2041-8213/ac9b27>.
- 798 [13] Wendy L. Freedman. “Measurements of the Hubble Constant: Tensions in Perspective”. In:
799 *The Astrophysical Journal* 919.1 (Sept. 2021), p. 16. doi: [10.3847/1538-4357/ac0e95](https://doi.org/10.3847/1538-4357/ac0e95).
800 URL: <https://dx.doi.org/10.3847/1538-4357/ac0e95>.
- 801 [14] Jodi Cooley. “Dark Matter direct detection of classical WIMPs”. In: *SciPost Phys. Lect.
802 Notes* (2022), p. 55. doi: [10.21468/SciPostPhysLectNotes.55](https://doi.org/10.21468/SciPostPhysLectNotes.55). URL: <https://scipost.org/10.21468/SciPostPhysLectNotes.55>.
- 803 [15] “Search for new phenomena in events with an energetic jet and missing transverse momentum
804 in pp collisions at $\sqrt{s} = 13$ TeV with the ATLAS detector”. In: *Phys. Rev. D* 103
805 (11 July 2021), p. 112006. doi: [10.1103/PhysRevD.103.112006](https://doi.org/10.1103/PhysRevD.103.112006). URL: <https://link.aps.org/doi/10.1103/PhysRevD.103.112006>.
- 806 [16] *Jetting into the dark side: a precision search for dark matter*. website. July 2020. URL:
807 <https://atlas.cern/updates/briefing/precision-search-dark-matter>.
- 808 [17] Celine Armand et. al. “Combined dark matter searches towards dwarf spheroidal galaxies
809 with Fermi-LAT, HAWC, H.E.S.S., MAGIC, and VERITAS”. in: *Proceedings of Science*.
810 Vol. 395. Mar. 2022. doi: <https://doi.org/10.22323/1.395.0528>.
- 811 [18] Tracy R. Slatyer. “Les Houches Lectures on Indirect Detection of Dark Matter”. In: *SciPost
812 Phys. Lect. Notes* (2022), p. 53. doi: [10.21468/SciPostPhysLectNotes.53](https://doi.org/10.21468/SciPostPhysLectNotes.53). URL:
813 <https://scipost.org/10.21468/SciPostPhysLectNotes.53>.
- 814 [19] Christian W Bauer, Nicholas L. Rodd, and Bryan R. Webber. “Dark matter spectra from
815 the electroweak to the Planck scale”. In: *Journal of High Energy Physics* 2021.1029-8479
816 (June 2021). doi: [https://doi.org/10.1007/JHEP06\(2021\)121](https://doi.org/10.1007/JHEP06(2021)121).
- 817 [20] Riccardo Catena and Piero Ullio. “A novel determination of the local dark matter density”.
818 In: *Journal of Cosmology and Astroparticle Physics* 2010.08 (Aug. 2010), p. 004. doi:
819 [10.1088/1475-7516/2010/08/004](https://doi.org/10.1088/1475-7516/2010/08/004). URL: <https://dx.doi.org/10.1088/1475-7516/2010/08/004>.
- 820 [21] B. P. Abbott et al. “Observation of Gravitational Waves from a Binary Black Hole Merger”.
821 In: *Phys. Rev. Lett.* 116 (6 Feb. 2016), p. 061102. doi: [10.1103/PhysRevLett.116.061102](https://doi.org/10.1103/PhysRevLett.116.061102). URL: <https://link.aps.org/doi/10.1103/PhysRevLett.116.061102>.
- 822 [22] R. Abbasi et. al. “Observation of high-energy neutrinos from the Galactic plane”. In: *Science*
823 380.6652 (June 2023), pp. 1338–1343.
- 824 [23] NASA Goddard Space Flight Center. *Fermi’s 12-year view of the gamma-ray sky*. website.

- 829 2022. URL: <https://svs.gsfc.nasa.gov/14090>.
- 830 [24] Marco Cirelli et al. “PPPC 4 DM ID: a poor particle physicist cookbook for dark matter
831 indirect detection”. In: *Journal of Cosmology and Astroparticle Physics* 2011.03 (Mar.
832 2011), p. 051. doi: [10.1088/1475-7516/2011/03/051](https://doi.org/10.1088/1475-7516/2011/03/051). URL: <https://dx.doi.org/10.1088/1475-7516/2011/03/051>.
- 834 [25] W. B. Atwood et al. “The Large Area Telescope on the Fermi Gamma-Ray Space Telescope
835 Mission”. In: *apj* 697.2 (June 2009), pp. 1071–1102. doi: [10.1088/0004-637X/697/2/1071](https://doi.org/10.1088/0004-637X/697/2/1071). arXiv: [0902.1089 \[astro-ph.IM\]](https://arxiv.org/abs/0902.1089).
- 837 [26] M. Ackermann et al. “Searching for Dark Matter Annihilation from Milky Way Dwarf
838 Spheroidal Galaxies with Six Years of Fermi Large Area Telescope Data”. In: *prl* 115.23,
839 231301 (Dec. 2015), p. 231301. doi: [10.1103/PhysRevLett.115.231301](https://doi.org/10.1103/PhysRevLett.115.231301). arXiv:
840 [1503.02641 \[astro-ph.HE\]](https://arxiv.org/abs/1503.02641).
- 841 [27] Mattia Di Mauro, Martin Stref, and Francesca Calore. “Investigating the effect of Milky
842 Way dwarf spheroidal galaxies extension on dark matter searches with Fermi-LAT data”.
843 In: *Phys. Rev. D* 106 (12 Dec. 2022), p. 123032. doi: [10.1103/PhysRevD.106.123032](https://doi.org/10.1103/PhysRevD.106.123032).
844 URL: <https://link.aps.org/doi/10.1103/PhysRevD.106.123032>.
- 845 [28] F. et al. Aharonian. “Observations of the Crab Nebula with H.E.S.S.”. In: *Astron. Astrophys.*
846 457 (2006), pp. 899–915. doi: [10.1051/0004-6361:20065351](https://doi.org/10.1051/0004-6361:20065351). arXiv: [astro-ph/0607333](https://arxiv.org/abs/astro-ph/0607333).
- 848 [29] J. Albert et al. “VHE γ -Ray Observation of the Crab Nebula and its Pulsar with the MAGIC
849 Telescope”. In: *The Astrophysical Journal* 674.2 (Feb. 2008), p. 1037. doi: [10.1086/525270](https://doi.org/10.1086/525270). URL: <https://dx.doi.org/10.1086/525270>.
- 851 [30] N. Park. “Performance of the VERITAS experiment”. In: *Proceedings, 34th International
852 Cosmic Ray Conference (ICRC2015): The Hague, The Netherlands, July, 30th July - 6th
853 August*. Vol. 34. 2015, p. 771. arXiv: [1508.07070 \[astro-ph.IM\]](https://arxiv.org/abs/1508.07070).
- 854 [31] A. Abramowski et al. “H.E.S.S. constraints on Dark Matter annihilations towards the Sculptor
855 and Carina Dwarf Galaxies”. In: *Astropart. Phys.* 34 (2011), pp. 608–616. doi: [10.1016/j.astropartphys.2010.12.006](https://doi.org/10.1016/j.astropartphys.2010.12.006). arXiv: [1012.5602 \[astro-ph.HE\]](https://arxiv.org/abs/1012.5602).
- 857 [32] A. Abramowski et al. “Search for dark matter annihilation signatures in H.E.S.S. observations
858 of Dwarf Spheroidal Galaxies”. In: *Phys. Rev. D* 90 (2014), p. 112012. doi: [10.1103/PhysRevD.90.112012](https://doi.org/10.1103/PhysRevD.90.112012). arXiv: [1410.2589 \[astro-ph.HE\]](https://arxiv.org/abs/1410.2589).
- 860 [33] H. Abdalla et al. “Searches for gamma-ray lines and ‘pure WIMP’ spectra from Dark
861 Matter annihilations in dwarf galaxies with H.E.S.S”. in: *JCAP* 11 (2018), p. 037. doi:
862 [10.1088/1475-7516/2018/11/037](https://doi.org/10.1088/1475-7516/2018/11/037). arXiv: [1810.00995 \[astro-ph.HE\]](https://arxiv.org/abs/1810.00995).

- 863 [34] J. Aleksić et al. “Optimized dark matter searches in deep observations of Segue 1 with
864 MAGIC”. in: *JCAP* 1402 (2014), p. 008. doi: [10.1088/1475-7516/2014/02/008](https://doi.org/10.1088/1475-7516/2014/02/008).
865 arXiv: [1312.1535 \[hep-ph\]](https://arxiv.org/abs/1312.1535).
- 866 [35] V.A. Acciari et al. “Combined searches for dark matter in dwarf spheroidal galaxies observed
867 with the MAGIC telescopes, including new data from Coma Berenices and Draco”. In:
868 *Physics of the Dark Universe* (2021), p. 100912. ISSN: 2212-6864. doi: <https://doi.org/10.1016/j.dark.2021.100912>. URL: <https://www.sciencedirect.com/science/article/pii/S2212686421001370>.
- 871 [36] M. L. Ahnen et al. “Indirect dark matter searches in the dwarf satellite galaxy Ursa Major II
872 with the MAGIC Telescopes”. In: *JCAP* 1803.03 (2018), p. 009. doi: [10.1088/1475-7516/2018/03/009](https://doi.org/10.1088/1475-7516/2018/03/009). arXiv: [1712.03095 \[astro-ph.HE\]](https://arxiv.org/abs/1712.03095).
- 874 [37] S. et al. Archambault. “Dark matter constraints from a joint analysis of dwarf Spheroidal
875 galaxy observations with VERITAS”. in: *prd* 95.8 (Apr. 2017). doi: [10.1103/PhysRevD.95.082001](https://doi.org/10.1103/PhysRevD.95.082001). arXiv: [1703.04937 \[astro-ph.HE\]](https://arxiv.org/abs/1703.04937).
- 877 [38] Louise Oakes et al. “Combined Dark Matter searches towards dwarf spheroidal galaxies with
878 Fermi-LAT, HAWC, HESS, MAGIC and VERITAS”. in: *Proceedings of Science*. 2019.
- 879 [39] Celine Armand et al. on behalf of the Fermi-LAT, HAWC, HESS, MAGIC, VERITAS.
880 “Combined Dark Matter searches towards dwarf spheroidal galaxies with Fermi-LAT,
881 HAWC, HESS, MAGIC and VERITAS”. in: *Proceedings of Science*. 2021.
- 882 [40] Daniel Kerszberg et al. on behalf of the Fermi-LAT, HAWC, HESS, MAGIC, and VER-
883 TIAS collaborations. “Search for dark matter annihilation with a combined analysis of
884 dwarf spheroidal galaxies from Fermi-LAT, HAWC, H.E.S.S., MAGIC and VERITAS”. in:
885 *Proceedings of Science*. 2023.
- 886 [41] A. U. Abeysekara et al. “Observation of the Crab Nebula with the HAWC Gamma-Ray
887 Observatory”. In: *The Astrophysical Journal* 843.1 (June 2017), p. 39. doi: [10.3847/1538-4357/aa7555](https://doi.org/10.3847/1538-4357/aa7555). URL: <https://doi.org/10.3847/1538-4357/aa7555>.
- 889 [42] Giacomo Vianello et al. *The Multi-Mission Maximum Likelihood framework (3ML)*. 2015.
890 arXiv: [1507.08343 \[astro-ph.HE\]](https://arxiv.org/abs/1507.08343).
- 891 [43] Marco Cirelli et al. “PPPC 4 DM ID: a poor particle physicist cookbook for dark matter
892 indirect detection”. In: *Journal of Cosmology and Astroparticle Physics* 2011.03 (Mar.
893 2011). ISSN: 1475-7516. doi: [10.1088/1475-7516/2011/03/051](https://doi.org/10.1088/1475-7516/2011/03/051). URL: <http://dx.doi.org/10.1088/1475-7516/2011/03/051>.
- 895 [44] Alex Geringer-Sameth, Savvas M. Koushiappas, and Matthew Walker. “DWARF GALAXY
896 ANNIHILATION AND DECAY EMISSION PROFILES FOR DARK MATTER EXPERI-
897 MENTS”. in: *The Astrophysical Journal* 801.2 (Mar. 2015), p. 74. ISSN: 1538-4357. doi:

- 898 10.1088/0004-637X/801/2/74. URL: <http://dx.doi.org/10.1088/0004-637X/80>
899 1/2/74.
- 900 [45] A. Albert et al. “Dark Matter Limits from Dwarf Spheroidal Galaxies with the HAWC
901 Gamma-Ray Observatory”. In: *The Astrophysical Journal* 853.2 (Feb. 2018), p. 154. ISSN:
902 1538-4357. doi: 10.3847/1538-4357/aaa6d8. URL: <http://dx.doi.org/10.3847/1538-4357/aaa6d8>.
- 904 [46] V. Bonnivard et al. “Spherical Jeans analysis for dark matter indirect detection in dwarf
905 spheroidal galaxies - Impact of physical parameters and triaxiality”. In: *Mon. Not. Roy.
906 Astron. Soc.* 446 (2015), pp. 3002–3021. doi: 10.1093/mnras/stu2296. arXiv:
907 1407.7822 [astro-ph.HE].
- 908 [47] Alex Geringer-Sameth and Matthew Koushiappas Savvas M. and Walker. “Dwarf galaxy
909 annihilation and decay emission profiles for dark matter experiments”. In: *Astrophys.
910 J.* 801.2 (2015), p. 74. doi: 10.1088/0004-637X/801/2/74. arXiv: 1408.0002
911 [astro-ph.CO].
- 912 [48] M. Ackermann et al. “Searching for Dark Matter Annihilation from Milky Way Dwarf
913 Spheroidal Galaxies with Six Years of Fermi Large Area Telescope Data”. In: *prl* 115.23,
914 231301 (Dec. 2015), p. 231301. doi: 10.1103/PhysRevLett.115.231301. arXiv:
915 1503.02641 [astro-ph.HE].
- 916 [49] A. et al. Albert. “Searching for Dark Matter Annihilation in Recently Discovered Milky Way
917 Satellites with Fermi-LAT”. in: *Astrophys. J.* 834.2 (2017), p. 110. doi: 10.3847/1538-4
918 357/834/2/110. arXiv: 1611.03184 [astro-ph.HE].
- 919 [50] Mattia Di Mauro and Martin Wolfgang Winkler. “Multimessenger constraints on the dark
920 matter interpretation of the Fermi-LAT Galactic Center excess”. In: *prd* 103.12, 123005
921 (June 2021), p. 123005. doi: 10.1103/PhysRevD.103.123005. arXiv: 2101.11027
922 [astro-ph.HE].
- 923 [51] V. Bonnivard et al. “Dark matter annihilation and decay in dwarf spheroidal galaxies: The
924 classical and ultrafaint dSphs”. In: *Mon. Not. Roy. Astron. Soc.* 453.1 (2015), pp. 849–867.
925 doi: 10.1093/mnras/stv1601. arXiv: 1504.02048 [astro-ph.HE].
- 926 [52] Gianfranco Bertone, Dan Hooper, and Joseph Silk. “Particle dark matter: evidence, can-
927 didates and constraints”. In: *Physics Reports* 405.5-6 (Jan. 2005), pp. 279–390. ISSN:
928 0370-1573. doi: 10.1016/j.physrep.2004.08.031. URL: <http://dx.doi.org/10.1016/j.physrep.2004.08.031>.
- 930 [53] HongSheng Zhao. “Analytical models for galactic nuclei”. In: *Mon. Not. Roy. Astron. Soc.*
931 278 (1996), pp. 488–496. doi: 10.1093/mnras/278.2.488. arXiv: astro-ph/9509122
932 [astro-ph].

- 933 [54] H. C. Plummer. “On the Problem of Distribution in Globular Star Clusters: (Plate 8.)”
934 In: *Monthly Notices of the Royal Astronomical Society* 71.5 (Mar. 1911), pp. 460–470.
935 ISSN: 0035-8711. doi: [10.1093/mnras/71.5.460](https://doi.org/10.1093/mnras/71.5.460). eprint: <https://academic.oup.com/mnras/article-pdf/71/5/460/2937497/mnras71-0460.pdf>. URL:
936 <https://doi.org/10.1093/mnras/71.5.460>.
- 937
938 [55] Daniel R. Hunter. “Derivation of the anisotropy profile, constraints on the local velocity
939 dispersion, and implications for direct detection”. In: *JCAP* 02 (2014), p. 023. doi:
940 [10.1088/1475-7516/2014/02/023](https://doi.org/10.1088/1475-7516/2014/02/023). arXiv: [1311.0256 \[astro-ph.CO\]](https://arxiv.org/abs/1311.0256).
- 941 [56] Barun Kumar Dhar and Liliya L. R. Williams. “Surface mass density of the Einasto family
942 of dark matter haloes: are they Sersic-like?” In: *Mon. Not. Roy. Astron. Soc.* (2010). doi:
943 [10.1111/j.1365-2966.2010.16446.x](https://doi.org/10.1111/j.1365-2966.2010.16446.x).
- 944 [57] M. Baes and E. Van Hese. “Dynamical models with a general anisotropy profile”. In: *Astron. Astrophys.* 471 (2007), p. 419. doi: [10.1051/0004-6361:20077672](https://doi.org/10.1051/0004-6361:20077672). arXiv:
945 [0705.4109 \[astro-ph\]](https://arxiv.org/abs/0705.4109).
- 946
947 [58] Matthew G. Walker, Edward W. Olszewski, and Mario Mateo. “Bayesian analysis of re-
948 solved stellar spectra: application to MMT/Hectochelle observations of the Draco dwarf
949 spheroidal”. In: *mnras* 448.3 (Apr. 2015), pp. 2717–2732. doi: [10.1093/mnras/stv099](https://doi.org/10.1093/mnras/stv099).
950 arXiv: [1503.02589 \[astro-ph.GA\]](https://arxiv.org/abs/1503.02589).